




Natural Allanite Reference Materials for *In Situ* U-Th-Pb and Sm-Nd Isotopic Measurements by LA-(MC)-ICP-MS

Ming Yang (1, 2, 3) , Yue-Heng Yang (1, 2, 3)* , Sandra L. Kamo (4), Rolf L. Romer (5), Nick M.W. Roberts (6), Hao Wang (1, 2, 3) , Lie-Wen Xie (1, 2), Chao Huang (1, 2), Jin-Hui Yang (1, 2, 3) and Fu-Yuan Wu (1, 2, 3)

(1) State Key Laboratory of Lithospheric Evolution, Institute of Geology and Geophysics, Chinese Academy of Sciences, Beijing 100029, China

(2) Innovation Academy of Earth Science, Chinese Academy of Sciences, Beijing 100029, China

(3) College of Earth and Planetary Sciences, University of Chinese Academy of Sciences, Beijing 100049, China

(4) Jack Satterly Geochronology Laboratory, Department of Earth Sciences, University of Toronto, 22 Ursula Franklin Street, Toronto, Ontario, M5S 3B1, Canada

(5) GFZ German Research Centre for Geosciences, Telegrafenberg, Potsdam 14473, Germany

(6) Geochronology and Tracers Facility, British Geological Survey, Keyworth, Nottingham NG12 5GG, UK

* Corresponding author. e-mail: yangyueheng@mail.iggcas.ac.cn

Allanite is a common accessory mineral that generally incorporates considerable amounts of Th, U and light rare Earth elements in its structure, making it a useful mineral for *in situ* U-Th-Pb geochronology and Sm-Nd isotope measurements. Here, we present *in situ* U-Th-Pb ages and Sm-Nd isotopic compositions for nine allanite samples considered as potential reference materials (CAP^b, Tara, Daibosatsu, LE40010, LE2808, A007, A011, A012 and SQ-51), with ages ranging from ~ 2650 Ma to ~ 12 Ma. Our study indicates that Daibosatsu and LE40010 have relatively homogeneous ¹⁴⁷Sm/¹⁴⁴Nd and ¹⁴³Nd/¹⁴⁴Nd isotopic compositions (¹⁴⁷Sm/¹⁴⁴Nd ratio variation is less than 2%) and, thus, can serve as primary reference materials for Sm-Nd microanalysis. In contrast, CAP^b, Tara, LE2808, A007, A011 and A012 all show homogeneous calculated initial ¹⁴³Nd/¹⁴⁴Nd isotopic compositions, but with variable ¹⁴⁷Sm/¹⁴⁴Nd compositions, and thus can be used only as secondary reference materials for Sm-Nd microanalysis. Of these materials, LE40010 allanite can serve as a suitable primary reference material for *in situ* U-Pb dating, CAP^b allanite can serve as a suitable primary reference material for *in situ* Th-Pb dating, and LE2808, LE40010, A007, A011 and A012 can serve as suitable secondary reference materials for *in situ* U-Pb geochronology. In addition, Daibosatsu is suitable as a secondary reference material for Cenozoic Th-Pb dating to monitor data reproducibility.

Keywords: allanite, U-Th-Pb dating, Sm-Nd isotope measurement, reference materials.

Received 10 Aug 21 – Accepted 16 Dec 21

Allanite, an epidote-group mineral, occurs in igneous, metamorphic and sedimentary rocks and hydrothermal systems (Gieré and Sorensen 2004). The general chemical formula for the epidote-group mineral is $A_2M_3Si_3O_{12}(OH)$, with the A site hosting Ca^{2+} , Sr^{2+} , Pb^{2+} , Mn^{2+} , Th^{4+} , U^{4+} and REE³⁺ and the M site being mostly occupied by Al^{3+} , Fe^{3+} , Fe^{2+} , Mn^{3+} , Mn^{2+} , Mg^{2+} , Cr^{3+} and V^{3+} (Dollase 1971, Gieré and Sorensen 2004). Allanite has high contents of LREE (light rare earth elements), Th and U, which render it suitable for U-Th-Pb dating and Nd isotope measurement.

Accessory minerals record important petrological information that improve our knowledge of magmatic processes

(Wones 1989, Robinson and Miller 1999, Schaltegger and Davies 2017). Allanite is a common accessory mineral in intermediate and acid magmatic rocks and forms solid solutions with epidote and clinozoisite (Gromet and Silver 1983, Petrik *et al.* 1995, Gieré and Sorensen 2004, Oberli *et al.* 2004, Beard *et al.* 2006, Cox *et al.* 2012). Allanite has been used as an indicator of oxygen fugacity (Gu 1989), as a monitor for the degree of magmatic crystallisation and fractionation (Barth *et al.* 1989, Oberli *et al.* 2004, Gregory *et al.* 2012), to constrain the age of igneous intrusions (Catlos *et al.* 2000, Spürigin *et al.* 2009, Gregory *et al.* 2012, Walters *et al.* 2013, Searle *et al.* 2016, Guo *et al.* 2014, 2017) and to determine the age of volcanic

events (Cox *et al.* 2012). Metamorphic allanite grains grow at *P-T* conditions that range from lower greenschist and amphibolite facies to high pressure and ultra-high pressure eclogite facies (Hermann 2002, Wing *et al.* 2003, Romer and Xiao 2005, Parrish *et al.* 2006, Smye *et al.* 2011, Thakur *et al.* 2018) and can be used to date a range of protoliths at variable metamorphic conditions (Janots *et al.* 2009, Rubatto *et al.* 2011, Smye *et al.* 2011, Vonlanthen *et al.* 2012, Boston *et al.* 2017, Engi 2017). Whole rock CaO and LREE contents control the stability of allanite during prograde stages of metamorphism (Wing *et al.* 2003, Janots *et al.* 2009, 2012). In particular, Ca is known to destabilise monazite to form allanite (Lee and Bastron 1967, Montel 1993). Allanite is the main carrier of LREE and Th in subduction zones and controls the redistribution of REE during subduction of continental rocks (Bea 1996, Hermann 2002, Spandler *et al.* 2003, Klimm *et al.* 2008, Rubatto *et al.* 2011, Soder and Romer 2018). Furthermore, allanite has been reported to occur in hydrothermal systems, especially skarn and IOCG (iron-oxide copper gold) deposits (Oliver *et al.* 1999, Chen and Zhou 2014, Deng *et al.* 2014, Fu *et al.* 2017, Li *et al.* 2018). By combining trace element data, isotopic analyses (in particular Nd and Sr) and U-Th-Pb dating of allanite, we can potentially and directly constrain the source of ore-forming materials, the properties of the ore-forming fluid and the timing of mineralisation (Gieré 1986, Oliver *et al.* 1999, Smith *et al.* 2009, Li *et al.* 2010, 2015, 2018, Chen and Zhou 2014, Deng *et al.* 2014, Zhu *et al.* 2015, Fu *et al.* 2017).

U-Th-Pb ages and Sm-Nd isotopic data can be obtained using traditional isotope dilution thermal ionisation mass spectrometry (ID-TIMS) methods, which is the benchmark technique for U-Th-Pb and Sm-Nd isotope analysis. However, bulk analysis of single crystals can obscure information in natural allanite that may have complex chemical and isotopic zonation (Catlos *et al.* 2000, Cox *et al.* 2003, Romer and Xiao 2005, Rubatto *et al.* 2011). Previous studies mainly concentrated on development of protocols for *in situ* allanite geochronology by SIMS (Catlos *et al.* 2000, Gregory *et al.* 2007, Liao *et al.* 2020) and LA-ICP-MS (Cox *et al.* 2003, Gregory *et al.* 2007, Darling *et al.* 2012, Korh 2014, McFarlane 2016, Bum *et al.* 2017). LA-ICP-MS U-Th-Pb dating is widely employed due to its good spatial resolution (usually ~ 10–50 μm), adequate precision (typically < 3% on individual $^{206}\text{Pb}/^{238}\text{U}$ and $^{208}\text{Pb}/^{232}\text{Th}$ measurements), rapid analysis (in the order of several minutes per spot) and low cost compared with other microanalytical techniques (e.g., SIMS; Catlos *et al.* 2000, Gregory *et al.* 2007, Liao *et al.* 2020). *In situ* Sm-Nd isotope measurement by laser ablation multi-collector (MC) ICP-MS has been shown to be feasible for allanite and other LREE-

enriched accessory minerals (Foster and Vance 2006, McFarlane and McCulloch 2007, Yang *et al.* 2008, Gregory *et al.* 2009, Fisher *et al.* 2011). A growing number of studies *in situ* Sm-Nd isotope measurement of allanite demonstrate the wide application and significance of this mineral (Spandler *et al.* 2018, Hammerli *et al.* 2019, Su *et al.* 2021).

There are numerous well-characterised zircon, monazite, apatite and titanite reference materials available for U-Pb, Hf, Sr and/or Nd isotopic analysis (Wiedenbeck *et al.* 2004, Wu *et al.* 2006, Sláma *et al.* 2008, Fisher *et al.* 2011, Iizuka *et al.* 2011, Liu *et al.* 2012, Yang *et al.* 2014, 2019, Li *et al.* 2015, Spandler *et al.* 2016, Ma *et al.* 2019). In contrast, there are only a few established allanite reference materials available for U-Th-Pb dating or for data quality control in Sm-Nd isotope analysis (e.g., Tara, CAP, AVC, LE40010, LE2808, Siss and Bona for U-Th-Pb dating (Gregory *et al.* 2007, Smye *et al.* 2014, Bum *et al.* 2017, Liao *et al.* 2020) and Daibosatsu for Sm-Nd isotopic analysis (McFarlane and McCulloch 2007, 2008). Despite the advent of high throughput *in situ* analytical methods, allanite geochronology reference materials are in short supply. Furthermore, growing application of *in situ* allanite Sm-Nd isotope analysis by LA-MC-ICP-MS brings about a need for a range of homogeneous Sm-Nd reference materials. For most available allanite reference materials, the Nd isotopic composition has not been reported. McFarlane and McCulloch (2007, 2008) reported the first LA-MC-ICP-MS Sm-Nd isotope data for the allanite sample Daibosatsu ($^{147}\text{Sm}/^{144}\text{Nd}$ and $^{143}\text{Nd}/^{144}\text{Nd}$ are 0.0825 and 0.512568 respectively). Their result was confirmed by ID-TIMS and other laser ablation studies (Fisher *et al.* 2011, Hammerli *et al.* 2014, 2019, Spandler *et al.* 2018). Among established allanite reference materials for geochronology, the Sm-Nd isotopic composition of Siss allanite was studied by *in situ* methods. Siss allanite, however, has variable Sm-Nd isotope composition (Gregory *et al.* 2009), in line with the results of ID-TIMS analyses (von Blanckenburg 1992).

The main purpose of this study is to test potential allanite reference materials (CAP^b, Tara, Daibosatsu, LE40010, LE2808, A007, A011, A012 and SQ-51) for *in situ* Sm-Nd isotope analysis and U-Th-Pb dating and, thereby, to establish a suite of well-characterised allanite minerals that will be made available to the geochemical community.

Allanite samples

Allanite samples, with ages ranging from ca. 2650 to ca. 12 Ma, from nine different areas were investigated. Brief

information on the investigated allanite samples is given in Table 1.

Tara

The Tara allanite was collected from a granodiorite of the Berridale Batholith, southeast Australia, and was described by Gregory *et al.* (2007), and further characterised by Smye *et al.* (2014). The dark brown and vitreous allanite grains are 100–300 µm in size and show only minor compositional variation. Alterations and inclusions are rare in our imagery (Figure 1b), but observed and described by Smye *et al.* (2014), including the presence of thorite. Gregory *et al.* (2007) presented SHRIMP and LA-ICP-MS analysis of the Tara allanite, yielding a weighted mean $^{208}\text{Pb}/^{232}\text{Th}$ age of 414.9 ± 3.3 Ma and single-spot mean $^{208}\text{Pb}/^{232}\text{Th}$ age of 417.5 ± 1.4 Ma respectively. The SHRIMP analysis gave a mean $^{206}\text{Pb}/^{238}\text{U}$ age of 419.3 ± 7.7 Ma. These ages are in good agreement with the Tara zircon age of 418.7 ± 4.2 Ma determined by U-Pb SHRIMP analysis (Ickert and Williams 2011), and thus, Tara was proposed as a suitable RM for U-Th-Pb geochronology by Gregory

et al. (2007). Subsequent studies have largely reproduced the age of Tara allanite (Darling *et al.* 2012, Smye *et al.* 2014, Burn *et al.* 2017). The U-Pb ID-TIMS data obtained by Smye *et al.* (2014) show a large age variation (440–400 Ma) possibly caused by later hydrothermal alteration. Following characterisation of individual grains using SEM imagery, it was concluded that Tara allanite can potentially serve as a reference material for U-Th-Pb dating (Smye *et al.* 2014, Burn *et al.* 2017).

CAP^b

The CAP^b allanite sample studied here is the same sample studied by Burn *et al.* (2017) and was collected from the same location as the CAP allanite. The CAP allanite originates from the Permian Cima D'Asta pluton, northern Italy, and was first dated by Barth *et al.* (1994) by Th-Pb ID-TIMS, yielding a weighted mean $^{208}\text{Pb}/^{232}\text{Th}$ age of 275 ± 1.5 Ma (2s, $n = 4$). Even though the pluton had been overprinted by Triassic regional hydrothermal alteration, the Th-Pb system of CAP^b allanite apparently remained unaffected. SIMS (Catlos *et al.* 2000, Gregory *et al.* 2007,

Table 1.
Summary information of allanite samples investigated in this study

Sample	Location	Reference age (Ma)	Reference	$^{143}\text{Nd}/^{144}\text{Nd}$ (2s)	Reference
Tara	Berridale Batholith, southeast Australia	414.9 ± 3.3^1 414.4 ± 6.4^2 411.3 ± 1.4^2 416.3 ± 1.9^2 $440\text{--}400^3$	Gregory <i>et al.</i> (2007) Burn <i>et al.</i> (2017) Darling <i>et al.</i> (2012) Smye <i>et al.</i> (2014)	No reference value	
CAP ^b	Permian Cima D'Asta pluton, northern Italy	275.0 ± 1.5^3 275.0 ± 4.3^1	Barth <i>et al.</i> (1994) Liao <i>et al.</i> (2020)		
Daibosatsu	Daibosatsu Pass, Yamanashi, Japan	11.5 ± 0.2^1	Liao <i>et al.</i> (2020)	0.512560 (10) ⁴ 0.512599 (13) ⁵ 0.512578 (26) ⁵ 0.512597 (12) ⁵ 0.512578 (9) ⁵	McFarlane and McCulloch (2007) Fisher <i>et al.</i> (2011) Fisher <i>et al.</i> (2011) Spandler <i>et al.</i> (2018) Hammerli <i>et al.</i> (2019)
LE40010	Fiskenaesset anorthosite complex, western Greenland.	2646 ± 94^3	Smye <i>et al.</i> (2014)	No reference value	
LE2808	Unknown	$1060\text{--}1100^3$	Smye <i>et al.</i> (2014)		
A007	Riddarhyttan area of Bergslagen, Sweden	No reference value			
A011	Pacoima Canyon pegmatite, southern California (USA)	1006 ± 37^1	Catlos <i>et al.</i> (2000)		
A012	Großhartmannsdorf, Saxony, Germany	No reference value			
SQ-51	Sin Quyen Fe-Cu-REE-Au-(U) deposit, north-western Vietnam	778.3 ± 9.2^1 $822\text{--}831^1$	Liao <i>et al.</i> (2020)		

These reference values were reported by previous studies and obtained by using ¹SIMS, ²LA-ICP-MS, ³ID-TIMS, ⁴solution-based MC-ICP-MS and ⁵LA-MC-ICP-MS.

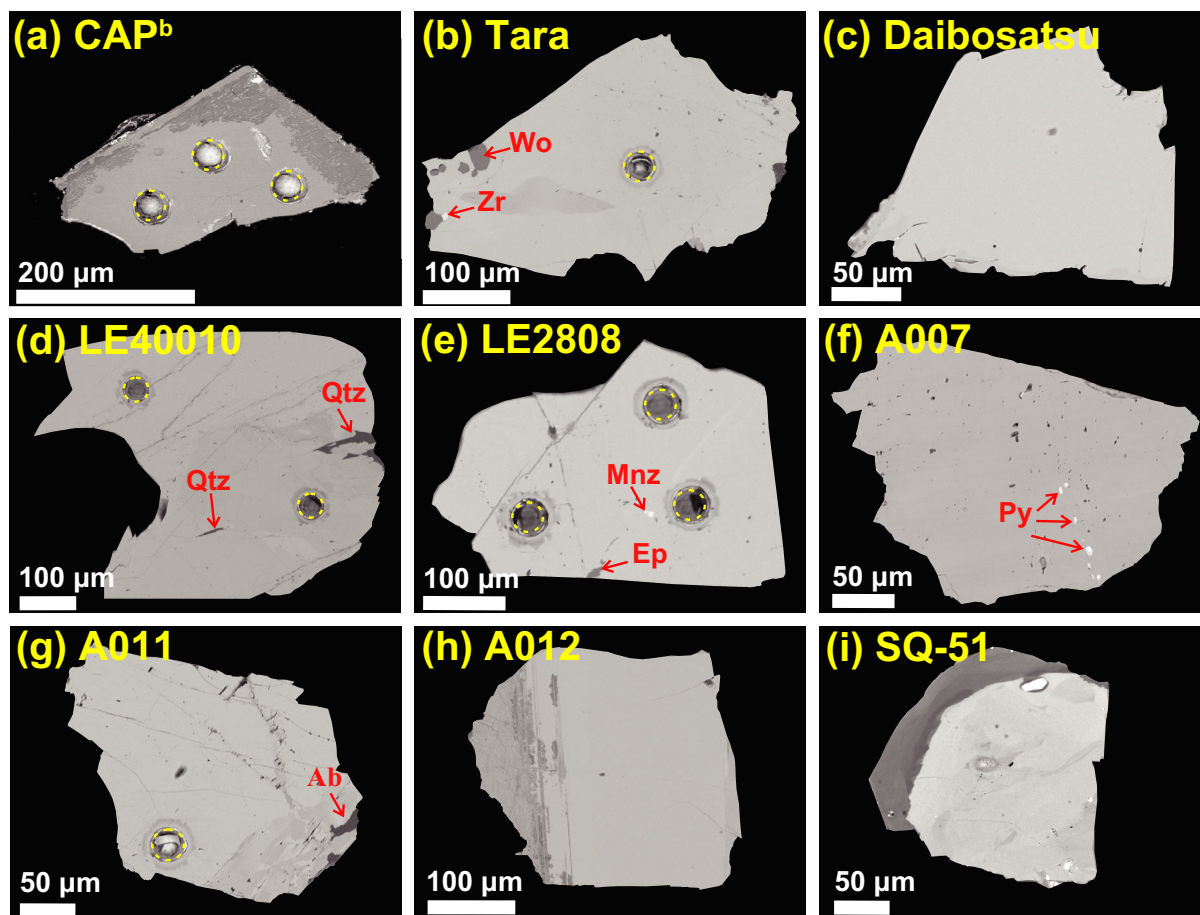


Figure 1. Representative back-scattered electron (BSE) images. Yellow dashed circles represent laser pits. Ab, albite; Ep, epidote; Mnz, monazite; Py, pyrite; Qtz, quartz; Wo, wollastonite.

Liao *et al.* 2020) and LA-ICP-MS (Burn *et al.* 2017) dating results of CAP^b allanite reproduced the TIMS age within uncertainty. The ²⁰⁷Pb-corrected ²⁰⁶Pb/²³⁸U results obtained via SIMS (Gregory *et al.* 2007), however, show more scatter and discordance compared with the ²⁰⁸Pb/²³²Th ages.

Daibosatsu

The Daibosatsu allanite originates from a *ca.* 13 Ma granitic pegmatite at Daibosatsu Pass, Yamanashi, Japan (Hoshino *et al.* 2005). The allanite crystals are dark brown, vitreous and vary in size. The grains have a homogeneous major element distribution (Hoshino *et al.* 2005). SIMS analysis of Daibosatsu allanite gave a weighted mean ²⁰⁸Pb/²³²Th age of 11.5 ± 0.2 Ma and a Tera-Wasserburg intercept age of 9.3 ± 3.0 Ma (Liao *et al.* 2020). McFarlane and McCulloch (2007, 2008) reported solution MC-ICP-MS ¹⁴³Nd/¹⁴⁴Nd data for the Daibosatsu allanite of 0.512559 ± 0.000010 and 0.512560 ± 0.000010, which is in good agreement with the *in situ* ¹⁴³Nd/¹⁴⁴Nd

data of 0.512564 ± 0.000008 (2s, n = 5) and 0.512568 ± 0.000010 (2s, n = 4). Fisher *et al.* (2011) measured the Nd isotopic composition of Daibosatsu allanite using ID-TIMS and LA-ICP-MS and obtained mean ¹⁴⁷Sm/¹⁴⁴Nd and ¹⁴³Nd/¹⁴⁴Nd ratios of 0.0767 ± 0.0037 (2s, n = 8) and 0.512599 ± 0.000013 (2s, n = 8), respectively, for ID-TIMS, and 0.0790 ± 0.0055 (2s, n = 20) 0.512578 ± 0.000026 (2s, n = 66), respectively, for LA-MC-ICP-MS. The mean ε_{Nd}(t) value is -1.3 ± 0.2 (McFarlane and McCulloch 2007). Later, Spandler *et al.* (2018) and Hammerli *et al.* (2019) used Daibosatsu allanite as secondary reference material and reported ¹⁴³Nd/¹⁴⁴Nd data of 0.512597 ± 0.000012 (2s, n = 8) and 0.512578 ± 0.000009 (2s, n = 3) respectively.

LE40010

Allanite LE40010 was previously investigated by Smye *et al.* (2014). This allanite is a megacryst collected from a quartz pegmatite from the late Archaean Fiskenaesset

Table 2.
Major element composition (% m/m) of the studied allanite samples obtained by EPMA, and atomic proportions

Allanite	CAP ^b n = 16		Tara n = 26		Daibosatsu n = 20		LE40010* n = 38		A007 n = 15		A011 n = 19		A012 n = 16		SQ-51 n = 21	
	Mean	2s	Mean	2s	Mean	2s	Mean	2s	Mean	2s	Mean	2s	Mean	2s	Mean	2s
SiO ₂	31.53	0.89	31.59	0.56	31.29	0.89	32.91	0.90	31.44	0.74	31.42	1.02	32.38	1.02	33.37	1.18
Al ₂ O ₃	15.43	1.22	13.90	0.70	14.40	0.43	18.58	1.57	14.39	1.85	14.07	2.03	16.20	0.54	16.68	1.00
CaO	9.97	1.48	10.36	0.52	8.81	0.28	12.63	1.67	10.85	1.45	10.34	1.96	12.19	1.81	14.77	1.12
MgO	0.84	0.23	1.31	0.16	0.36	0.04	1.29	0.72	0.92	0.40	0.31	0.30	0.94	0.07	0.18	0.06
FeO	12.84	2.08	14.16	1.04	15.78	0.40	11.76	0.87	14.40	1.49	15.52	1.30	12.76	0.68	15.09	0.73
MnO	0.57	0.39	0.77	0.13	1.06	0.05	0.32	0.15	0.29	0.09	0.70	0.14	0.46	0.13	0.13	0.06
TiO ₂	0.91	0.33	1.08	0.22	0.91	0.05	0.19	0.09	0.24	0.07	0.93	0.39	0.43	0.12	0.43	0.10
ZnO	0.02	0.07	0.03	0.07	0.02	0.05	N/A	N/A	0.02	0.06	0.04	0.07	0.02	0.07	0.01	0.05
SnO	0.18	0.15	0.17	0.14	0.16	0.13	N/A	N/A	0.14	0.15	0.17	0.13	0.16	0.12	0.14	0.10
Y ₂ O ₃	0.34	0.35	0.19	0.48	0.53	0.07	0.05	0.01	0.78	0.63	0.25	0.53	0.39	0.43	0.10	0.18
La ₂ O ₃	5.40	1.30	6.08	1.59	6.42	0.22	5.29	0.68	5.33	1.01	7.06	2.16	3.83	0.22	5.39	0.68
Ce ₂ O ₃	10.59	1.53	11.02	1.04	12.08	0.30	9.93	1.35	8.91	1.88	11.03	2.27	8.51	0.40	8.00	1.01
Pr ₂ O ₃	1.12	0.17	1.04	0.20	0.94	0.12	1.40	0.19	1.08	0.29	0.89	0.17	0.90	0.17	0.61	0.17
Nd ₂ O ₃	4.10	0.43	3.26	0.69	2.68	0.20	2.77	0.36	4.81	0.98	2.53	0.29	3.25	0.51	1.56	0.16
Sm ₂ O ₃	0.53	0.25	0.30	0.30	0.35	0.25	0.55	0.07	0.95	0.39	0.21	0.19	0.54	0.36	0.11	0.19
Gd ₂ O ₃	1.66	0.20	1.51	0.11	1.70	0.11	0.69	0.09	1.91	0.29	1.50	0.18	1.46	0.25	1.06	0.16
Dy ₂ O ₃	0.09	0.21	0.05	0.15	0.12	0.28	N/A	N/A	0.15	0.27	0.09	0.22	0.11	0.20	0.03	0.11
ThO ₂	1.51	0.93	1.13	0.52	1.04	0.16	2.20	0.36	0.01	0.03	0.51	0.25	1.08	0.32	0.04	0.08
Total	97.64	2.85	97.94	2.15	98.64	2.31	100.58	1.15	96.62	1.61	97.56	1.86	95.62	2.69	97.71	2.56

Atomic proportions based on 12.5 O and the sum of cations normalised to 8

Si	3.050	3.036	2.973	2.981	3.041	3.041	3.041	3.062	3.040
Al	1.758	1.575	1.978	1.491	1.604	1.639	1.806	1.746	
Ca	1.034	1.066	1.222	0.901	1.071	1.124	1.234	1.411	
Mg	0.121	0.188	0.174	N/A	0.044	0.132	0.133	0.047	
Fe ²⁺	0.937	0.811	0.610	1.039	0.935	0.769	0.703	0.592	
Fe ³⁺	0.102	0.327	0.279	0.398	0.322	0.396	0.306	0.585	
Mn	0.047	0.062	0.025	0.142	0.057	0.024	0.037	0.011	
Ti	0.066	0.078	0.013	0.071	0.068	0.017	0.031	0.029	
Zn	0.002	0.002	N/A	N/A	0.003	0.001	0.001	0.001	
Sr	0.010	0.010	N/A	N/A	0.010	0.008	0.009	0.007	

Table 2 (continued).
Major element composition (% m/m) of the studied allanite samples obtained by EPMA, and atomic proportions

Atomic proportions based on 12.5 O and the sum of cations normalised to 8											
Y	0.017	0.010	0.027	0.002	0.074	0.040	0.013	0.020	0.005		
La	0.192	0.216	0.230	0.176	0.135	0.190	0.253	0.134	0.172		
Ce	0.375	0.388	0.429	0.329	0.376	0.316	0.392	0.295	0.253		
Pr	0.039	0.036	0.033	0.046	0.062	0.038	0.031	0.031	0.019		
Nd	0.142	0.112	0.093	0.090	0.185	0.166	0.088	0.110	0.048		
Sm	0.018	0.010	0.012	0.017	0.066	0.032	0.007	0.018	0.003		
Gd	0.053	0.048	0.055	0.021	0.030	0.061	0.048	0.046	0.030		
Dy	0.003	0.002	0.004	N/A	0.022	0.005	0.003	0.004	0.001		
Th	0.033	0.025	0.023	0.045	0.029	0.001	0.011	0.023	0.001		
Total	8.000	8.000	8.000	8.000	8.000	8.000	8.000	8.000	8.000		
Fe ³⁺ /Fe _T	0.094	0.286	0.172	0.314	0.276	0.340	0.257	0.303	0.497		

Totals do not include water, which is likely to be 1–2% m/m.

Fe³⁺/Fe_T was calculated by charge balance on the basis of 8 cations and 12.5 oxygens.

*EPMA, previously published in Smye *et al.* (2014).

'n' represents the number of analyses.

N/A, not available.

anorthosite complex, western Greenland. The previous study showed that the U-Pb systematics of LE40010 exhibits scatter and yields sub-concordant apparent U-Pb ID-TIMS ages ranging from 2750 to 2600 Ma. The $^{207}\text{Pb}/^{235}\text{U}$ data scatter less and yield a mean age of 2646 ± 94 Ma. For comparison, the mean $^{206}\text{Pb}/^{238}\text{U}$ age is 2735 ± 226 Ma (Smye *et al.* 2014).

LE2808

Allanite LE2808 is a megacryst from a pegmatite and has been studied by Smye *et al.* (2014). See Smye *et al.* (2014) for geological background information available for this allanite sample. Similar to LE40010, this crystal experienced hydrothermal alteration. Allanite LE2808 exhibits extreme discordance between apparent $^{238}\text{U}/^{206}\text{Pb}$ and $^{232}\text{Th}/^{208}\text{Pb}$ ages; in particular, the $^{208}\text{Pb}/^{232}\text{Th}$ results were highly scattered. Common Pb corrected $^{206}\text{Pb}/^{238}\text{U}$ and $^{207}\text{Pb}/^{235}\text{U}$ ages range between 1060 and 1100 Ma (Smye *et al.* 2014).

A007

Sample A007 was collected from the Bastnäs-type REE deposit in the Riddarhyttan area of Bergslagen, Sweden. Bastnäs-type mineralisation has been described by Holtstam *et al.* (2014) and Linders (2016). The main ore-bearing units in the Bergslagen ore district are rhyolitic to rhyodacitic, alkali-rich metavolcanic rocks (Stephens and Jansson 2020). Magmatic activity with associated mineralisation started at ~ 1.9 Ga. Molybdenite Re-Os ages obtained from Bastnäs-type deposits ranges from 1900 to 1840 Ma (Holtstam *et al.* 2014).

A011

The Pacoima Canyon pegmatite, southern California (USA), is known as ‘allanite pegmatite’ (Silver *et al.* 1963). Allanite A011 was sampled from this pegmatite. The U-Pb ID-TIMS zircon age of the pegmatite is 1190 Ma (Silver *et al.* 1963, Barth *et al.* 1995). Catlos *et al.* (2000) presented an *in situ* Th-Pb ion-microprobe age of 1006 ± 37 Ma (1s; two spots on one grain) for allanite from the Pacoima Canyon pegmatite. Their age is distinctly younger than the age reported by Silver *et al.* (1963) and Barth *et al.* (1995). Catlos *et al.* (2000) interpreted the age discrepancy to reflect Pb diffusion in allanite during the cooling of the pegmatite.

A012

Sample A012 was collected from Großhartmannsdorf, Saxony, Germany. Regionally, the sample location lies within that part of the Saxo-Thuringian Zone, that is the Erzgebirge that

experienced medium- to high-grade metamorphism during the Variscan orogeny. The Erzgebirge represents a stack of metamorphic nappes of crustal rocks that have reached medium to high and ultra-high pressure conditions at ~ 340 Ma and that were stacked and exhumed within a few millions of years (Rötzler and Plessen 2010, Kroner and Romer 2013). The nappes were in the upper crust when they were intruded by 327 Ma old and younger granites (Förster and Romer 2010).

SQ-51

SQ-51 allanite was collected from the Sin Quyen Fe-Cu-REE-Au-(U) deposit, which is hosted in the Phan Si Pan belt of north-western Vietnam. The Phan Si Pan belt consists of a metamorphic complex intruded by Neoproterozoic igneous rocks (Gas'kov *et al.* 2012, Zhu *et al.* 2015). The deposit contains abundant Fe, Cu and REE, associated with subordinate Au and U, and is hosted in Proterozoic metapelites. The age of the massive and banded replacement ores is bracketed by the ages of hydrothermal zircon and monazite and a post-mineralisation granitic dyke (Li *et al.* 2018). Hydrothermal zircon and monazite yield indistinguishable U-Pb ages of 841 ± 12 and 836 ± 18 Ma, respectively, whereas zircon from the granitic dyke yields a weighted mean $^{206}\text{Pb}/^{238}\text{U}$ age of 736 ± 7 Ma (Li *et al.* 2018). Allanite from this deposit gave two SIMS U-Pb ages of *ca.* 780 Ma and *ca.* 830 Ma (Liao *et al.* 2020).

Analytical methods

All allanite samples were separated using a Frantz magnetic separator and were concentrated using heavy liquids. They were then selected by hand picking under a binocular microscope. Some separated grains were embedded in a 1-inch epoxy mount, sectioned to expose their interior, polished and mapped by optical microscopy. Chemical and isotopic homogeneity was investigated by electron probe microanalysis (EPMA) and laser ablation ICP-MS (LA-ICP-MS) analyses, respectively, at the State Key Laboratory of Lithospheric Evolution, Institute of Geology and Geophysics, Chinese Academy of Sciences (IGGCAS). Some relatively homogeneous samples were selected for U-Pb ID-TIMS analysis at the Jack Satterly Geochronology Laboratory, Department of Earth Sciences, University of Toronto, Canada and at GFZ German Research Centre for Geosciences, Germany.

Chemical characterisation

Electron probe microanalysis: Backscattered electron (BSE) imaging of allanite was completed using a Nova NanoSEM 450 field-emission scanning electron microscope

(FSEM) and a JEOL JXA8300 Electron Microprobe to characterise internal structures and mineral inclusions. Quantitative major element analysis of allanite minerals was performed on a CAMECA SX Five Electron Microprobe housed at Electron Microprobe and Scanning Electron Microscope Laboratory, IGGCAS, Beijing. The operating conditions for the CAMECA SX Five were a 3×10^{-8} A beam current, 15 kV acceleration voltage and 5 μm beam size. The peak counting time was 20 s for all elements, and the background counting time was 10 s on the high- and low-energy background positions. Natural minerals, synthetic oxides and glasses were used as reference materials.

Isotopic characterisation

U-Pb ID-TIMS dating: U-Pb ID-TIMS analyses of allanite were conducted at the Jack Satterly Geochronology Laboratory, Department of Earth Sciences, University of Toronto (Canada) and at GFZ German Research Centre for Geosciences, Potsdam (Germany).

Samples A007, A011 and A012 were analysed at the Jack Satterly Geochronology Laboratory (JSGL). All grains were washed in nitric acid at room temperature, and loaded into PTFE dissolution capsules with $\sim 120 \mu\text{l}$ 50% HF and $\sim 20 \mu\text{l}$ HNO₃ mixed with a ^{205}Pb - ^{235}U isotopic tracer solution. Grains were dissolved in an oven at 195 °C for ~ 4 days. Samples were dried to a precipitate and re-dissolved in $\sim 0.15 \text{ ml}$ 3.1 mol l⁻¹ HCl at 195 °C overnight prior to loading into anion exchange columns (Krogh 1973). An HBr chemical separation procedure was performed to isolate Pb and U, which was evaporated to a small droplet in H₃PO₄ and loaded onto outgassed Re filaments with silica gel (Gerstenberger and Haase 1997). Uranium and Pb were determined with a VG354 mass spectrometer using either a Daly detector in pulse counting dynamic mode, or in multiple Faraday cups in static measurement mode with ^{204}Pb in the axial Daly detector. For data acquisition, either VG Sector software or an in-house Visual Basic program was used. The $^{206}\text{Pb}/^{238}\text{U}$ and $^{207}\text{Pb}/^{206}\text{Pb}$ ratios and apparent ages were corrected for initial ^{230}Th disequilibrium assuming a Th/U ratio in the magma of 4.2. Procedural blanks were assumed to be 1 pg Pb and 0.1 pg U. Initial common Pb was corrected using the Pb evolution model of Stacey and Kramers (1975). The mass discrimination correction for the Daly detector is constant at 0.05% per atomic mass unit. Amplifier gains and Daly characteristics were monitored using the SRM 982 Pb reference material. Decay constants are those of Jaffey *et al.* (1971) and recommended by IUGS (Hiess *et al.* 2012): $\lambda^{238}\text{U} = 1.55125 \times 10^{-10} \text{ year}^{-1}$; $\lambda^{235}\text{U} = 9.8485 \times 10^{-10} \text{ year}^{-1}$; $^{238}\text{U}/^{235}\text{U} = 137.818$. U-Pb data reduction and age

calculations were performed using an in-house Visual Basic programs written by D.W. Davis. All age uncertainties quoted in the text and tables, and ellipses in concordia diagrams are given at the 95% confidence level. Plotting and discordia calculation were conducted using Isoplot 3.0 (Ludwig 2003).

Sample A007 was also analysed at the GFZ German Research Centre for Geosciences, Potsdam (GFZ). To remove surface contamination, the samples were rinsed in warm 1 mol l⁻¹ HNO₃ for 30 min, and then, the samples were rinsed with H₂O and acetone. A mixed ^{205}Pb - ^{235}U tracer was added before sample dissolution. The samples were dissolved in 40% HF on a hotplate at 160 °C for three days. The U and Pb separation was adapted from the HBr-HCl analytical procedure described in Romer and Lüders (2006). Uranium and Pb were loaded with H₃PO₄ and silica gel on the same Re filaments. The isotopic ratios of U and Pb were measured using a Triton TIMS instrument operated in static or dynamic multi-collection mode using Faraday collectors and an ion counter, depending on the signal intensity. Lead was analysed at 1200–1260 °C and U at 1360–1430 °C. Data reduction followed the procedures described by Schmid *et al.* (2003). Initial $^{206}\text{Pb}/^{204}\text{Pb}$ ratio was estimated using the typical Pb isotopic compositions of Svecofennian massif sulphide ores (Romer and Wright 1993). The initial $^{207}\text{Pb}/^{204}\text{Pb}$ was estimated using the $^{207}\text{Pb}/^{204}\text{Pb}$ vs. $^{206}\text{Pb}/^{204}\text{Pb}$ diagram. Uncertainties in tables and the text are given at the 95% confidence level. Assuming the procedural blank for Pb and U are 15 pg and 1 pg respectively. The data were plotted using Isoplot 3.0 (Ludwig 2003).

In situ trace element and U-Th-Pb age determinations: Trace element contents and U-Th-Pb ages were determined using an Agilent 7500a quadrupole (Q)-ICP-MS instrument coupled to a 193 nm ArF excimer laser ablation systems or a 257 nm Yb diode femtosecond laser ablation system housed at IGGCAS, Beijing, China. Geolas HD (Coherent, Gottingen, Germany) and NWRFemto^{UC} (Electro Scientific Industries, Portland, United States) laser ablation systems were used in this study. Detailed information on Geolas HD and NWRFemto^{UC} is presented in Wu *et al.* (2020).

The Pulse/Analogue (P/A) factor of the detector was calibrated using a standard tuning solution before conducting the experiments. During laser ablation, the instrument was optimised using NIST SRM 610 glass reference material. Helium was used as the carrier gas and mixed with argon prior to entering the ICP torch. The parameters of the two gases were optimised to obtain stable maximum

signal intensity for $^{238}\text{U}^+$, while suppressing oxide formation and limiting fractionation between U and Th, which were monitored using ThO^+/Th^+ ($< 0.5\%$) and Th/U ratio (to approximately 1). Detailed parameter settings are presented in Table 2. A fluence of $\sim 5 \text{ J cm}^{-2}$, spot size of $\sim 40\text{--}60 \mu\text{m}$ and repetition rate of 8 Hz were used for measurement. All LA-ICP-MS measurements were carried out using time-resolved analysis in fast, peak jumping mode. The dwell time for each isotope was set at 6 ms for ^{43}Ca , ^{49}Ti , ^{55}Mn , ^{85}Rb , ^{88}Sr , ^{89}Y , ^{92}Zr , ^{178}Hf and REE, 10 ms for ^{232}Th and ^{238}U , 15 ms for ^{204}Pb , ^{206}Pb and ^{208}Pb , and 30 ms for ^{207}Pb . Each spot analysis consists of an approximate 30 s background and a 60 s sample data acquisition. A matrix-matched allanite reference material (Tara) was used as the primary reference materials to correct $^{207}\text{Pb}/^{206}\text{Pb}$,

$^{206}\text{Pb}/^{238}\text{U}$, $^{207}\text{Pb}/^{235}\text{U}$ ($^{238}\text{U}/^{235}\text{U} = 137.818$) (Hiess *et al.* 2012) and $^{208}\text{Pb}/^{232}\text{Th}$ ratios. CAP^b (275 Ma; Barth *et al.* 1994) and Daibosatsu (11.5 Ma; Liao *et al.* 2020) were used as secondary reference materials to monitor data reproducibility. Trace element mass fractions were calibrated using Si as the internal standard element (SiO₂ contents were measured previously by EPMA) and using NIST SRM 610 (Jochum *et al.* 2011) as the primary reference material and NIST SRM 612 (Jochum *et al.* 2011) for data monitoring. Isotopic and elemental fractionation plus instrumental mass bias were corrected for using Glitter 4.0 software (Griffin *et al.* 2008). Signal sections of each analysis were selected independently to obtain similar intervals for reference materials and unknowns. The relative standard deviation of reference values for Tara allanite was set at 2%. The

Table 3.
Typical instrument parameters for U-Pb dating, trace element and Sm-Nd isotopic measurement

Laser ablation systems	Coherent Geolas HD	NWRFemto ^{UC}
Laser system	ComPex 102, ArF excimer UV 193 nm	Yb diode femtosecond laser ablation system, 257 nm
Ablation cell and volume	Standard barrel cell, volume ca. 4 cm ³	Two volume cell
Fluence	$\sim 5 \text{ J cm}^{-2}$ for trace elements and U-Pb dating, $\sim 6 \text{ J cm}^{-2}$ for Sm-Nd isotope measurement	
Repetition rate	8 Hz	
Spot diameter nominal	40 μm for trace elements and U-Pb dating, 24–32 μm for Sm-Nd isotope measurement	
Ablation duration	60 s for trace elements and U-Pb dating, 60 s for Sm-Nd isotope measurement	
Sampling mode	Static spot ablation	
Sample preparation	Conventional mineral separation, 1 inch resin mount	
Mass spectrometers	Thermo Fisher Neptune MC-ICP-MS	Agilent 7500a Q-ICP-MS
RF forward power	$\sim 1300 \text{ W}$	$\sim 1350 \text{ W}$
Carrier gas flow	$\sim 1.1 \text{ l min}^{-1}$	$\sim 1.1 \text{ l min}^{-1}$
Cool gas	16 l min^{-1}	Sample depth Interface cone
Auxiliary gas	0.8 l min^{-1}	$\sim 4.5 \text{ mm}$ Ni
N ₂ gas flow	4 ml min^{-1}	Dwell times
Sampling cone	Ni, aperture 1.0 mm	15 ms for ^{204}Pb , ^{206}Pb and ^{208}Pb , 30 ms for ^{207}Pb , 10 ms for ^{232}Th and ^{238}U , 6 ms for other elements
Skimmer cone	Ni, aperture 0.8 mm	Analysis duration
Sampling mode	9 blocks of 8 cycles for Nd (solution) 1 block of 40 cycles for Sm (solution) 1 block of 200 cycles (laser)	90 s (including 30 s background), 60 s ablation
Integration time	4 s for Nd (solution) 2 s for Sm (solution) 0.262 s (laser)	
Background/baseline	30 s on peak zero (OPZ)	

MC-ICP-MS cup configuration

Faraday cup	L4	L3	L2	L1	Centre	H1	H2	H3	H4
Nominal mass	142	143	144	145	146	147	148	149	150
Nd ⁺	$^{142}\text{Nd}^+$	$^{143}\text{Nd}^+$	$^{144}\text{Nd}^+$	$^{145}\text{Nd}^+$	$^{146}\text{Nd}^+$		$^{148}\text{Nd}^+$		$^{150}\text{Nd}^+$
[Ce ⁺ , Sm ⁺]	$^{142}\text{Ce}^+$		$^{144}\text{Sm}^+$			$^{147}\text{Sm}^+$	$^{148}\text{Sm}^+$	$^{149}\text{Sm}^+$	$^{150}\text{Sm}^+$

mode of data reduction depended on the common Pb composition, Th contents and the age of the analytical sample: (1) Samples with significant common Pb are reported as intercept dates in the Tera-Wasserburg diagram (all intercept ages in this study are derived from isochrons on a Tera-Wasserburg diagram unless otherwise stated.). Additionally, the weighted $^{206}\text{Pb}/^{238}\text{U}$ and $^{208}\text{Pb}/^{232}\text{Th}$ mean dates were calculated using a ^{207}Pb correction of common Pb, assuming a common Pb composition corresponding to the two-stage crustal Pb model of Stacey and Kramers (1975). (2) The Cenozoic sample with significant common Pb and considerable excess ^{206}Pb is only reported as a weighted $^{208}\text{Pb}/^{232}\text{Th}$ mean age calculated using the ^{207}Pb correction of common Pb, assuming a common Pb composition corresponding to the two-stage crustal Pb model of Stacey and Kramers (1975). Detailed data reduction methods can be found in Yang *et al.* (2014, 2019) and Liao *et al.* (2020). Uncertainties in tables and the text are given at the 95% confidence level. The additional systematic uncertainties were propagated onto the final ages following Horstwood *et al.* (2016) include the uncertainty of the common Pb composition, the decay constant uncertainty, the reference material uncertainty and laboratory-based long-term over-dispersion of the method (~ 2%). Age uncertainties quoted as age \pm x/y, where x is without systematic uncertainties, and y is with systematic uncertainties. The U-Th-Pb ages and weighted mean ages were calculated using the ISOPLOT 3.0 software package (Ludwig 2003).

In situ Sm-Nd isotope determination: All *in situ* isotope measurements for this study were carried out at the IGGCAS using a Thermo Scientific Neptune Plus MC-ICP-MS coupled to a 193 nm excimer laser system. Detailed instrument and analysis conditions are presented in Table 2. Prior to analysis, the instrument was tuned and optimised for maximum sensitivity using JNdi-1 standard solution. The laser fluence was set to ~ 6 J cm⁻² with a 4 Hz laser repetition rate and ~ 24–32 μm beam diameter, depending on the Nd mass fraction of the samples. Each spot analysis consisted of approximately 30 s baseline acquisition and 60 s data acquisition (Yang *et al.* 2008, Ma *et al.* 2019). Every ten sample analyses were followed by two analyses each of Daibosatsu ($^{147}\text{Sm}/^{144}\text{Nd} = 0.0767 \pm 0.0037$, $^{143}\text{Nd}/^{144}\text{Nd} = 0.511599 \pm 0.000013$, Fisher *et al.* 2011) and Tara allanite (no previously published ratios available) for external calibration and data monitoring.

To obtain accurate $^{147}\text{Sm}/^{144}\text{Nd}$ and $^{143}\text{Nd}/^{144}\text{Nd}$ isotope ratios using LA-MC-ICP-MS, the contribution of the isobaric interference of ^{144}Sm on the ^{144}Nd signal must be carefully corrected (Foster and Vance 2006, McFarlane and

McCulloch 2007, 2008, Yang *et al.* 2008, 2009, Fisher *et al.* 2011). In natural allanite, Sm/Nd generally ranges from 0.05 to 0.2, so ^{144}Sm can contribute ~ 2–6% to the measured ^{144}Nd signal. In this study, we used $^{147}\text{Sm}/^{149}\text{Sm} = 1.08680$, $^{144}\text{Sm}/^{149}\text{Sm} = 0.22332$ and $^{146}\text{Nd}/^{144}\text{Nd} = 0.7219$ (O’Nions *et al.* 1977, Dubois *et al.* 1992, Isnard *et al.* 2005). The measured $^{147}\text{Sm}/^{149}\text{Sm}$ ratio was used to calculate the Sm fractionation factor using the exponential law. The measured ^{147}Sm intensity was used to estimate the Sm interference on mass 144 by employing the natural $^{147}\text{Sm}/^{144}\text{Sm}$ ratio of 4.866559 (Isnard *et al.* 2005). In a second step, the interference-corrected $^{146}\text{Nd}/^{144}\text{Nd}$ ratio was used to calculate the Nd fractionation factor. Finally, the $^{143}\text{Nd}/^{144}\text{Nd}$ and $^{145}\text{Nd}/^{144}\text{Nd}$ ratios were normalised using the exponential law. True $^{147}\text{Sm}/^{144}\text{Nd}$ ratios were calculated using the exponential law after correcting for the isobaric interference of ^{144}Sm on ^{144}Nd . The $^{147}\text{Sm}/^{144}\text{Nd}$ ratio was externally calibrated against the $^{147}\text{Sm}/^{144}\text{Nd}$ ratio in the allanite reference material analysed during the same session (Yang *et al.* 2013, 2014, Lin *et al.* 2016). The $^{145}\text{Nd}/^{144}\text{Nd}$ value was also used as data quality control during the measurement (reference value $^{145}\text{Nd}/^{144}\text{Nd} = 0.348415 \pm 0.000007$, Wasserburg *et al.* 1981). Systematic uncertainties were propagated into the final $^{147}\text{Sm}/^{144}\text{Nd}$ and $^{143}\text{Nd}/^{144}\text{Nd}$ ratios. Long-term measurement uncertainty of $^{147}\text{Sm}/^{144}\text{Nd}$ and $^{143}\text{Nd}/^{144}\text{Nd}$ ratios were assumed to be at the 0.02% level (Gonçalves *et al.* 2018). The raw data were exported offline, and the whole data reduction was performed using a Microsoft Excel macro.

Solution Sm-Nd isotope measurement: All chemical preparation of allanite was undertaken on class 100 workbenches inside a class 1000 clean laboratory. Individual allanite crystal chips were washed in an ultrasonic bath in 2% HNO₃ for 15 min, then rinsed several times with high-purity (Milli-Q) H₂O (resistivity: 18.2 M Ω cm at 25 °C) from Millipore (USA) and finally dried. Approximately 20–30 mg of allanite crystals was weighed into a 7 ml round bottom SavillexTM Teflon/PTFE screw top capsule. Each aliquot was spiked with a weighed ^{149}Sm - ^{150}Nd enriched tracer and then digested using 0.1 ml concentrated HClO₄ and 1 ml concentrated HF. Neodymium and Sm were separated from matrix elements using a single stage TODGA resin (2 ml, 100–200 mesh). Detailed sample digestion and separation protocols are given by Chu *et al.* (2019).

Samarium and Nd mass fractions and $^{143}\text{Nd}/^{144}\text{Nd}$ isotope ratios were measured on a Thermo Fisher Scientific Neptune MC-ICP-MS at IGGCAS. The operational settings and cup configurations are summarised in Table 2. The

JNdi-1 Nd standard solution was used to evaluate the reproducibility and accuracy of the instrument during Sm-Nd isotope measurements. For Sm isotope determination, Alfa-Sm standard solution was used for mass bias correction of $^{147}\text{Sm}/^{149}\text{Sm}$ ratios. Detailed mass spectrometry and offline data reduction followed the procedure of Yang *et al.* (2011). Procedural blanks were less than 50 pg for Sm and Nd. Therefore, blank contributions are considered negligible and do not require corrections of the measured isotopic ratios.

To monitor analytical procedures, replicate analyses of certified reference material BCR-2 from the United States Geological Survey (USGS) and Chinese rock reference materials GSR-2 and GSR-3 were made using the procedure described above. During the period of data acquisition, BCR-2, GSR-2 and GSR-3 gave 0.512638 ± 0.000007 (2SE, $n = 1$), 0.512395 ± 0.000008 (2SE, $n = 1$) and 0.512909 ± 0.000010 (2SE, $n = 2$) for $^{143}\text{Nd}/^{144}\text{Nd}$ and 0.1382 ± 0.0003 (2SE, $n = 1$), 0.1099 ± 0.0002 (2SE, $n = 1$) and 0.1224 ± 0.0002 (2SE, $n = 2$) for $^{147}\text{Sm}/^{144}\text{Nd}$, respectively, which are identical within uncertainty with the recommended values (Weis *et al.* 2006, Chu *et al.* 2009, Yang *et al.* 2010, 2011, 2020, Fourny *et al.* 2016, Bao *et al.* 2018).

Results

Tara

Fragments of the Tara allanite are characterised by minimal internal zoning in BSE images and small mineral inclusions (Figure 1b). The high Ce_2O_3 (11.42% *m/m*) mass fraction makes it an allanite-(Ce). The next abundant REE is La_2O_3 (6.08% *m/m*), followed by Nd_2O_3 (3.12% *m/m*). Allanite contains considerable amounts of ThO_2 (1.13% *m/m*). Comparison between spots showed large variations for some oxides, especially for ThO_2 (> 40%) (Table 3). Trace element mass fractions determined by LA-ICP-MS (Table 4) show large variations. The chondrite-normalised REE patterns (Figure 2b) show a strong LREE enrichment with respect to the HREE and a negative Eu/Eu* anomaly (0.21–0.27). The sample also exhibits a large fractionation of LREE/HREE ($(\text{La}/\text{Lu})_{\text{N}} = 803$). The U mass fractions range from 39 to 94 $\mu\text{g g}^{-1}$, with a mean of 61 $\mu\text{g g}^{-1}$. The Th mass fractions range from 7460 to 18300 $\mu\text{g g}^{-1}$, with a mean of 11300 $\mu\text{g g}^{-1}$.

The LA-MC-ICP-MS Sm-Nd isotope measurements for the Tara allanite revealed variations in $^{147}\text{Sm}/^{144}\text{Nd}$ and $^{143}\text{Nd}/^{144}\text{Nd}$ from 0.0446 to 0.0982 and from 0.512033 to 0.512233 respectively. The mean $^{147}\text{Sm}/^{144}\text{Nd}$ and $^{143}\text{Nd}/^{144}\text{Nd}$ values were 0.0552 ± 0.0163 (2s,

$n = 112$) and 0.512090 ± 0.000061 (2s, $n = 112$). Although the $^{147}\text{Sm}/^{144}\text{Nd}$ ratio displayed large variation with the relative standard deviation (2RSD) of 29.5%, the calculated initial $^{143}\text{Nd}/^{144}\text{Nd}$ ratio of 112 analyses only showed limited variation (0.511940 ± 0.000038 , 2s, $n = 112$). All the data points fall on a 415 Ma reference isochron (Figure 3b) and yield a mean $\epsilon_{\text{Nd}}(t)$ of -3.18 ± 0.75 (2s, $n = 112$) (Table 7). Due to limited supply, the Sm-Nd isotope systematics of Tara allanite was not analysed by solution methods.

CAP^b

CAP^b allanite exhibits compositional zoning without inclusions in BSE images (Figure 1a). EPMA analyses indicate this sample is also abundant in LREE with Ce_2O_3 (10.59% *m/m*), La_2O_3 (5.40% *m/m*) and Nd_2O_3 (4.10% *m/m*). ThO_2 varies from 0.82 to 2.22% *m/m*, with a mean value of 1.51% *m/m* (Table 3). Trace element mass fractions of CAP^b allanite determined by LA-ICP-MS (Table 4) show large variations. The chondrite-normalised REE patterns (Figure 2b) show a strong LREE enrichment with respect to the HREE and a strong negative Eu/Eu* anomaly (0.02–0.07). The sample also exhibits a large fractionation of LREE/HREE ($(\text{La}/\text{Lu})_{\text{N}} = 476$). The sample contains less U and more Th, with U mass fractions ranging from 58 to 245 $\mu\text{g g}^{-1}$ and Th mass fractions ranging from 8510 to 15600 $\mu\text{g g}^{-1}$.

U-Th-Pb results of CAP^b allanite acquired by LA-ICP-MS defined an intercept age of 274.1 ± 6.7 Ma (2s; MSWD = 1.1, $n = 19$; Figure 4a) by forcing to a upper intercept $^{207}\text{Pb}/^{206}\text{Pb}$ ratio of 0.85 estimated using the model of Stacey and Kramers (1975) for crustal Pb evolution. When un-anchored, this dataset yields a regression with a $^{207}\text{Pb}/^{206}\text{Pb}$ intercept of 0.84 ± 0.09 and an age of 273.2 ± 9.7 Ma. All analyses gave ^{207}Pb -corrected weighted $^{206}\text{Pb}/^{238}\text{U}$ and $^{208}\text{Pb}/^{232}\text{Th}$ ages are $271.7 \pm 2.1/5.8$ Ma (2s; MSWD = 1.6, $n = 19$) and $270.8 \pm 3.8/6.6$ Ma (2s; MSWD = 0.7, $n = 19$) respectively. Common Pb fractions range from 1.16 to 5.09% for f_{208} and from 9.94 to 31.96% for f_{206} . CAP^b allanite was also used as secondary reference material, and the results are similar. The obtained U-Th-Pb ages of CAP^b allanite are in good agreement with previous ID-TIMS, SIMS and LA-ICP-MS results (Barth *et al.* 1994, Catlos *et al.* 2000, Gregory *et al.* 2007, Burn *et al.* 2017, Liao *et al.* 2020).

LA-MC-ICP-MS Sm-Nd analysis of this sample shows slight variations in $^{147}\text{Sm}/^{144}\text{Nd}$ and limited variation in $^{143}\text{Nd}/^{144}\text{Nd}$, ranging from 0.0642 to 0.0983 and from 0.512090 to 0.512180 respectively. All data points plot

Table 4.
Trace element measurement results for allanite samples measured by LA-ICP-MS

Element $\mu\text{g g}^{-1}$	NIST SRM 612 n = 54		CAP ^b n = 19		Tara n = 54		Daibosatsu n = 20		LE40010 n = 17		LE2808 n = 23		A007 n = 21		A011 n = 17		A012 n = 18		SQ-51 n = 23	
	Mean	2RSD%	Mean	2RSD%	Mean	2RSD%	Mean	2RSD%	Mean	2RSD%	Mean	2RSD%	Mean	2RSD%	Mean	2RSD%	Mean	2RSD%	Mean	2RSD%
⁴³ Ca	85600	7.2	72800	13.1	75900	9.6	61900	6.4	75200	4.9	61300	6.7	78900	8.4	75800	6.1	80400	58.7	103000	7.0
⁴⁹ Ti	44	8.4	4530	27.2	5550	29.0	4680	6.9	1080	6.1	5240	12.4	1590	61.4	5470	8.9	2530	31.8	2160	11.4
⁵⁵ Mn	38	11.8	3750	52.1	5690	21.8	7160	4.3	2160	5.0	13600	19.8	2350	45.3	5350	11.9	3550	32.1	925	18.2
⁸⁵ Rb	32	7.4	1	103	1	73.1	1	15.3	0	39.4	3	135	1	90.5	0	62.5	12	408	1	124
⁸⁸ Sr	80	8.9	35	53.2	98	138	4	81.2	67	9.0	3	70.0	61	70.6	66	168	233	310	147	51.0
⁸⁹ Y	39	15.4	2380	78.3	1220	49.4	3920	5.8	421	4.5	11800	12.8	6820	49.3	959	66.5	3870	74.4	630	122
⁹² Zr	39	15.5	3	17.4	3	133	6	31.5	2	17.4	3	44.5	3	187	8	31.2	2	159	8	62.8
¹³⁹ La	37	12.5	55000	19.5	69500	26.4	55400	6.8	37800	3.4	26600	12.6	63800	24.0	79900	11.4	39900	27.9	47900	15.6
¹⁴⁰ Ce	39	8.3	102000	10.6	116000	21.8	99000	6.9	72200	3.7	79200	7.4	99500	25.5	122000	5.1	85500	26.9	74400	14.3
¹⁴¹ Pr	39	10.5	10900	11.9	10800	24.8	7950	6.5	6890	3.6	11100	4.6	12300	21.7	9900	6.0	9460	27.5	5590	14.6
¹⁴⁶ Nd	37	11.9	38600	18.1	33400	29.9	24000	6.6	20700	4.0	45000	3.8	55900	17.8	27200	8.6	34300	28.7	13900	15.0
¹⁴⁷ Sm	39	12.8	5140	43.5	2570	34.5	3260	6.7	1860	4.1	8550	6.7	11200	17.2	1840	18.8	6410	36.1	835	19.7
¹⁵² Eu	36	10.7	51	39.2	125	23.5	7	24.2	77	4.7	18	9.5	537	62.8	88	52.9	121	47.6	356	24.3
¹⁵⁷ Gd	39	15.0	2320	55.3	1010	33.5	1980	7.2	692	3.9	5320	9.7	7310	34.3	751	20.9	3590	53.8	324	39.4
¹⁵⁹ Tb	39	14.0	228	68.3	88	39.0	235	6.4	48	3.8	633	11.3	523	46.6	66	33.9	380	63.7	30	80.6
¹⁶³ Dy	37	15.1	853	75.7	325	42.6	1030	7.4	156	4.3	2920	12.3	1650	50.6	255	43.6	1400	72.3	134	107
¹⁶⁵ Ho	40	14.8	113	75.5	46	44.6	156	6.8	18	4.5	448	12.6	148	45.6	38	51.0	158	75.5	23	118
¹⁶⁶ Er	39	15.9	210	79.6	96	44.7	325	6.5	32	5.5	1080	12.8	191	48.8	85	59.4	254	79.8	56	117
¹⁶⁹ Tm	38	15.3	22	93.9	11	46.3	39	6.8	3	6.0	142	13.6	14	56.1	11	74.0	22	83.0	7	116
¹⁷² Yb	40	13.9	132	108	72	45.4	245	6.4	14	5.3	921	15.2	64	630	75	82.0	112	82.8	44	110
¹⁷⁵ Lu	38	15.1	15	114	9	46.6	31	6.6	2	8.0	133	18.2	6	68.1	10	84.1	11	78.9	5	105
¹⁷⁸ Hf	38	15.5	0.3	73.5	0.4	140	1.2	40.7	0.3	52.7	0.6	46.5	0.2	37.3	0.6	39.7	0.6	311	0.6	68.6
²⁰⁴ Pb	39	8.5	10	37.3	4	86.8	9	16.6	7	54.1	11	31.3	5	80.2	8	60.5	5	145	2	82.8
Pb*	38	8.1	182	31.6	211	43.4	9	8.8	1980	6.3	596	19.2	18	69.7	303	35.9	175	20.1	86	54.5
²³² Th	39	13.3	11500	39.1	11300	51.8	9050	10.0	13900	6.5	10000	21.3	0	247	5190	32.6	13100	52.9	158	25.3
²³⁸ U	38	8.0	121	99.8	61	55.0	216	8.1	70	6.3	211	21.1	37	82.7	34	125	176	65.6	669	69.1
Th/U	1	12.6	111	69.6	190	36.0	42	9.5	200	3.1	48	15.9	0	286	175	53.9	77	36.5	0	88.1
REE+Y	575	12.9	218000	10.9	235000	23.5	198000	6.5	141000	3.6	194000	4.4	260000	631	243000	6.2	186000	26.5	144000	14.6
(La/Lu) _N	0.1	5.7	476	87.0	803	47.1	183	3.8	2400	7.7	21	30.9	1250	74.0	940	50.2	554	180	1520	133
Eu/Eu*	3	5.4	0.05	64.8	0.24	12.3	0.01	23.4	0.21	1.6	0.01	6.4	0.18	54.2	0.23	34.7	0.08	24.3	2.13	13.4

(La/Lu)_N was normalised to chondrite after Boynton (1984); Eu/Eu* = $\frac{Eu_N}{\sqrt{(Sm_N \times Gd_N)}}$ was normalised to chondrite after Boynton (1984).
Pb* ($\mu\text{g g}^{-1}$) = 23.6%²⁰⁴Pb ($\mu\text{g g}^{-1}$) + 22.6%²⁰⁷Pb ($\mu\text{g g}^{-1}$) + 52.3%²⁰⁸Pb ($\mu\text{g g}^{-1}$). Trace element mass fractions were calibrated against NIST SRM 610. All data presented as simple mean values. The individual data can be found in Table S2.
RSD, relative standard deviation.
n, number of analyses.

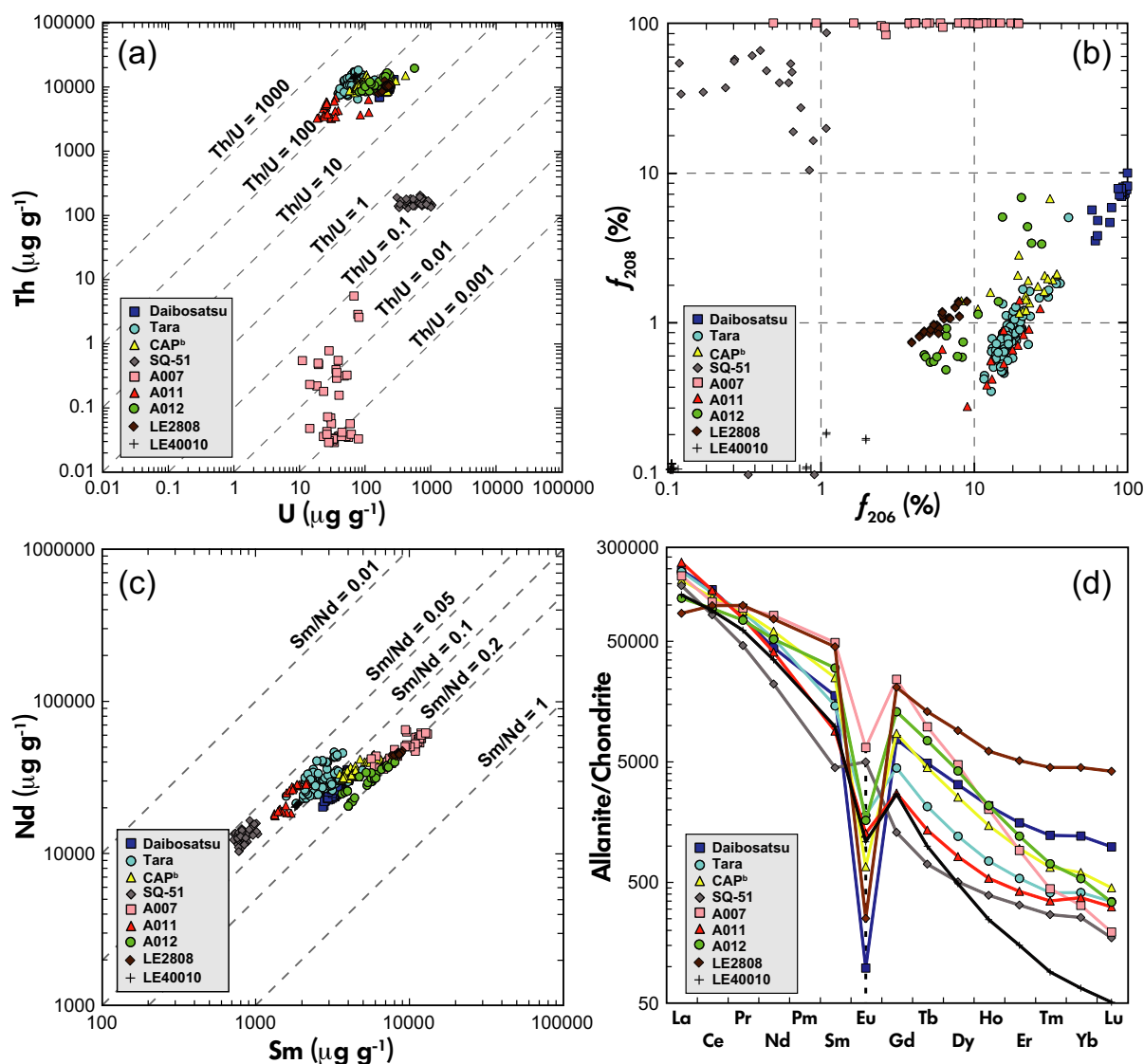


Figure 2. (a) Comparison between U and Th mass fractions. (b) The f_{206} and f_{208} values represent the percentage of common ^{206}Pb and ^{208}Pb in total ^{206}Pb and ^{208}Pb , respectively, of allanite samples analysed in this study. (c) Comparison between Sm and Nd mass fraction. (d) Mean chondrite-normalised REE distribution patterns.

along a reference isochron for 275 Ma (Figure 3a) and yield a mean $\epsilon_{\text{Nd}}(t)$ of -5.70 ± 0.72 ($2s$, $n = 51$) (Table 7). The calculated initial $^{143}\text{Nd}/^{144}\text{Nd}$ ratios of fifty-one analyses show only limited variation with a mean value of 0.511991 ± 0.000037 ($2s$, $n = 51$). By reason of the short supply of CAP^b allanite, and thus the quantities available at the time of measurement, it was not analysed by ID-MC-ICP-MS.

Daibosatsu

The Daibosatsu allanite typically is homogenous in BSE images (Figure 1c) with ThO_2 mass fractions obtained by EPMA of $1.04 \pm 0.16\%$ m/m ($2s$, $n = 20$). The high Ce_2O_3 (12.08% m/m) mass fraction makes it an allanite-

(Ce). The next abundant REE is La_2O_3 (6.42% m/m), followed by Nd_2O_3 (2.68% m/m) (Table 3). REE measurement results acquired by LA-ICP-MS show limited variation. Chondrite-normalised REE patterns (Figure 2c) show a strong enrichment in LREE. The Daibosatsu allanite also show a strong negative Eu anomaly ($\text{Eu}/\text{Eu}^* = 0.01$) and a strong fractionation between LREE and HREE ($(\text{La}/\text{Lu})_{\text{N}} = 183$). This sample shows U mass fractions ranging from 203 to 231 $\mu\text{g g}^{-1}$, and Th mass fractions from 8040 to 9580 $\mu\text{g g}^{-1}$ (Figure 5b). For the analysed fragments, the relative standard deviation of twenty analyses is ca. 6% for REE and ca. 9% for U and Th (Table 4), which indicates the trace element mass fractions are relatively homogeneous.

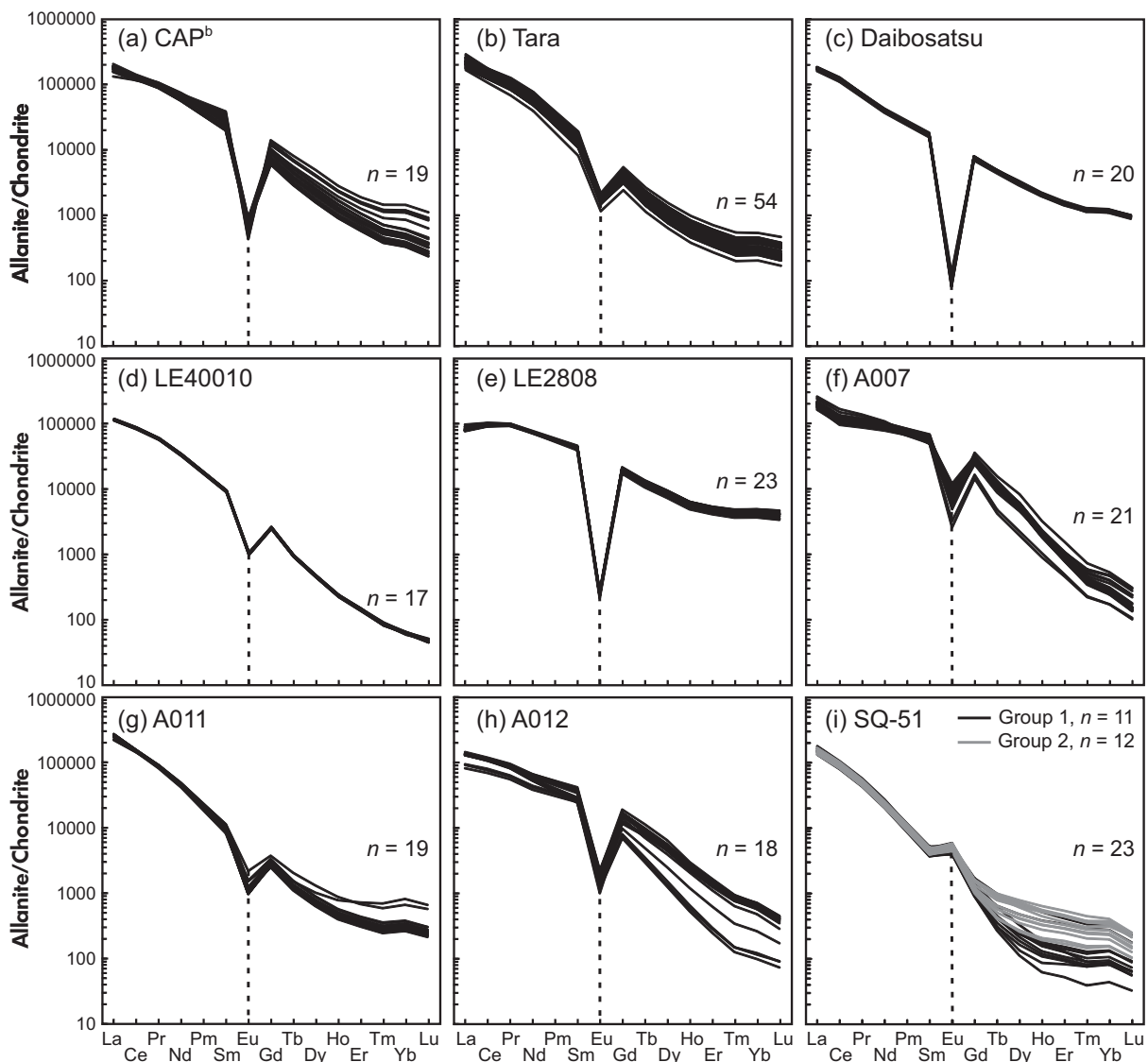


Figure 3. Individual chondrite-normalised REE distribution patterns of the nine allanite samples studied. Group 1 and Group 2 in (i) represent unaltered and altered domains of SQ-51 allanite. *n* represents the number of analyses.

The weighted mean $^{208}\text{Pb}/^{232}\text{Th}$ age obtained by LA-ICP-MS method is $11.6 \pm 0.3/0.4$ Ma ($2s$; $n = 20$; Figure 4b). The measured f_{208} ranges from 3.23% to 9.87%, whereas f_{206} is considerably higher with a mean of 81.83% ($2s$; $n = 20$; Table 5). The high proportion of common ^{206}Pb reflects the markedly lower U content and the young age of the sample. Because Th-rich Cenozoic allanite like Daibosatsu allanite have considerable contributions of excess ^{206}Pb , only the $^{208}\text{Pb}/^{232}\text{Th}$ ages are reported. The Daibosatsu allanite was also used as secondary reference material, and the results are similar. The obtained $^{208}\text{Pb}/^{232}\text{Th}$ age in this study agrees well with the reported SIMS $^{208}\text{Pb}/^{232}\text{Th}$ age of 11.5 ± 0.2 Ma (Liao *et al.* 2020).

The Sm-Nd isotope systematics of Daibosatsu allanite obtained by LA-MC-ICP-MS is homogeneous with a relative standard deviation of 1.97% for the measured $^{147}\text{Sm}/^{144}\text{Nd}$ ratio. Daibosatsu was used as primary reference material for *in situ* Sm-Nd isotope measurements in this study.

LE40010

LE40010 fragments show alteration and quartz inclusions in BSE images (Figure 1d). The sample is also rich in LREE with Ce_2O_3 (9.93% *m/m*), La_2O_3 (5.29% *m/m*) and Nd_2O_3 (2.77% *m/m*). The mean ThO_2 is 2.20% *m/m* (Table 3). The trace element mass fractions determined by

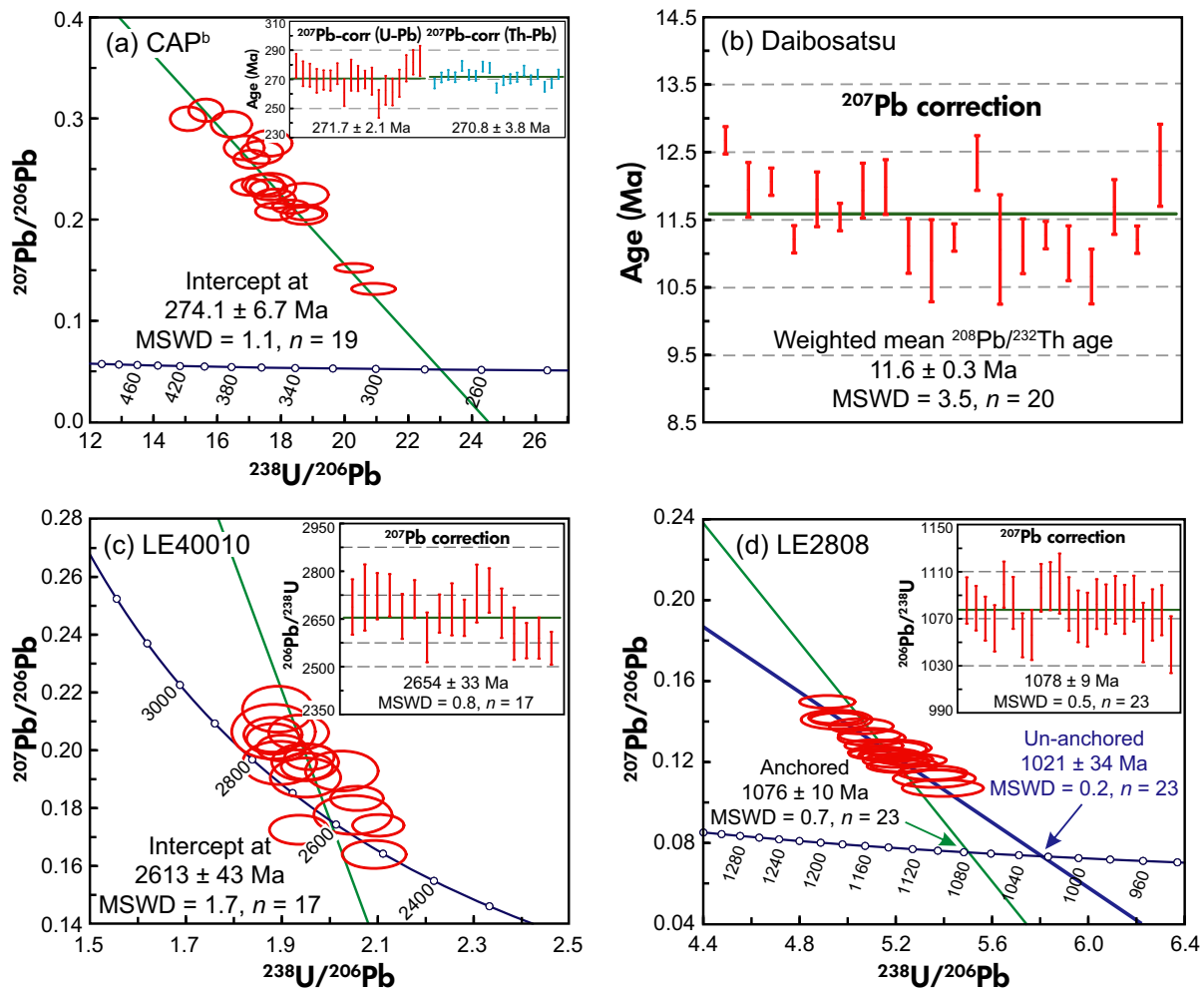


Figure 4. Tera-Wasserburg diagrams for (a) CAP^b, (c) LE40010 and (d) LE2808 allanite samples. Insets show weighted mean $^{206}\text{Pb}/^{238}\text{U}$ and $^{208}\text{Pb}/^{232}\text{Th}$ ages for sample CAP^b after ^{207}Pb correction and weighted mean $^{206}\text{Pb}/^{238}\text{U}$ ages for LE40010 and LE2808. (b) Daibosatsu allanite is geologically young, and its ^{206}Pb is dominated by common Pb. Therefore, only the weighted mean $^{208}\text{Pb}/^{232}\text{Th}$ age after ^{207}Pb correction is reported. Discordia in Tera-Wasserburg diagrams are forced to $^{207}\text{Pb}/^{206}\text{Pb}$ ratios estimated by the two-stage crustal Pb model of Stacey and Kramers (1975). The un-anchored intercept age of LE2808 allanite is also presented in (d). n represents the number of analyses. Ellipses represent the 95% confidence level.

LA-ICP-MS indicate LE40010 allanite is relatively homogeneous in REE, U, Th and Pb. The relative standard deviation is lower than 5%. The chondrite-normalised REE patterns reveal a strong enrichment in LREE (Figure 2d) and a strong fractionation between LREE and HREE ($(\text{La}/\text{Lu})_{\text{N}} = 2400$). It also shows a strong negative Eu anomaly ($\text{Eu}/\text{Eu}^* = 0.21$). The U and Th mass fractions range from 67 to 73 $\mu\text{g g}^{-1}$ and 13200 to 14500 $\mu\text{g g}^{-1}$ respectively. Both major and trace element mass fractions indicate LE40010 allanite is homogenous in chemical composition.

LE40010 is the most radiogenic sample with f_{206} ranging from 0.02 to 1.95% and f_{208} from 0.02 to 0.23% (Figure 5b). Most data cluster near the concordia curve and yield an

intercept at 2613 ± 43 Ma (2s, MSWD = 1.7, $n = 17$; Figure 4c) with an anchored $^{207}\text{Pb}/^{206}\text{Pb}$ ratio of 1.09, taken from the Stacey and Kramers (1975) model for 2600 Ma. A free regression of the dataset yields an upper $^{207}\text{Pb}/^{206}\text{Pb}$ ratio of 0.60 ± 0.14 and an intercept on concordia of 2521 ± 90 Ma (2s, MSWD = 1.1, $n = 17$). This upper intercept value ($^{207}\text{Pb}/^{206}\text{Pb} = 0.60 \pm 0.14$) is distinctly lower than the model contemporaneous $^{207}\text{Pb}/^{206}\text{Pb}$ ratio of 1.09, which may reflect a mixture between common and radiogenic Pb components. However, the analyses are very close to concordia and cannot constrain a reliable regression line. Therefore, the anchored $^{207}\text{Pb}/^{206}\text{Pb}$ ratio as estimated using the model of Stacey and Kramers (1975) was used in this study. The common Pb corrected weighted mean

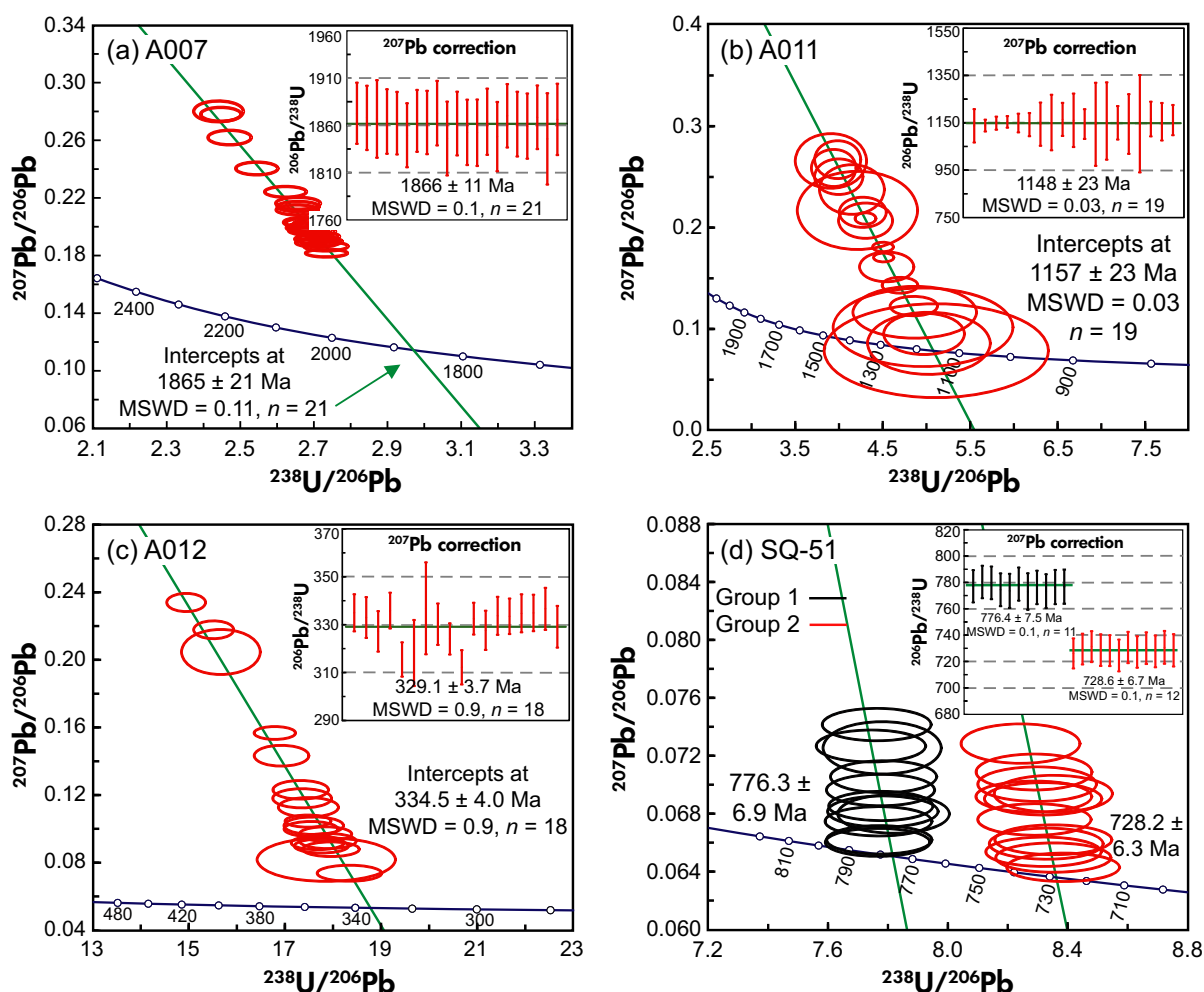


Figure 5. Tera-Wasserburg diagrams for allanite (a) A007, (b) A011, (c) A012 and (d) SQ-51. Insets show weighted mean $^{206}\text{Pb}/^{238}\text{U}$ ages after ^{207}Pb correction. Discordia in Tera-Wasserburg diagrams are forced to $^{207}\text{Pb}/^{206}\text{Pb}$ ratios estimated by the two-stage crustal Pb model of Stacey and Kramers (1975). n represents the number of analyses. Ellipses represent the 95% confidence level.

$^{206}\text{Pb}/^{238}\text{U}$ age is $2654 \pm 33/63$ Ma (2s, MSWD = 0.8, $n = 17$; Figure 4c). The Th-Pb systematics of LE40010 shows more scatter and a less well defined mean age of $2610 \pm 65/83$ Ma (2s, MSWD = 15, $n = 17$; Table 5). This result corresponds well with the published ID-TIMS $^{207}\text{Pb}/^{235}\text{U}$ mean age of 2646 ± 94 Ma (Smye *et al.* 2014).

The LA-MC-ICP-MS $^{147}\text{Sm}/^{144}\text{Nd}$ and $^{143}\text{Nd}/^{144}\text{Nd}$ ratios of LE40010 show limited variation and are 0.0543 ± 0.0007 (2s, $n = 52$) and 0.510105 ± 0.000035 (2s, $n = 52$) respectively. The mean $\epsilon_{\text{Nd}}(t)$ is 1.96 ± 0.66 (2s, $n = 52$). Two separate aliquots of LE40010 analysed by ID-MC-ICP-MS yield $^{147}\text{Sm}/^{144}\text{Nd}$ and $^{143}\text{Nd}/^{144}\text{Nd}$ values of 0.0569 ± 0.0002 (2s) and 0.510109 ± 0.000016 (2s), respectively, with a mean

$\epsilon_{\text{Nd}}(t)$ of 1.07 ± 0.22 (2s). The solution-based results agree with the laser ablation results within uncertainty.

LE2808

Inclusions like epidote and monazite are found in LE2808 fragments, and alteration along cracks was also observed (Figure 1e). EPMA data show that LE2808 allanite is abundant in LREE and Th with Ce_2O_3 (10.56% *m/m*), La_2O_3 (3.77% *m/m*), Nd_2O_3 (5.33% *m/m*) and ThO_2 (1.32% *m/m*) (Table 3). Chondrite-normalised REE patterns determined by LA-ICP-MS show enrichment in LREE, small fractionation between LREE and HREE ($(\text{La}/\text{Lu})_{\text{N}} = 21$), and strong negative Eu anomaly ($\text{Eu}/\text{Eu}^* = 0.01$). This sample contains Th mass fraction ranges from 7850 to 12400 $\mu\text{g g}^{-1}$, U mass fraction ranges from 161 to

Table 5.
Compilation of allanite U-Th-Pb ages obtained by LA-ICP-MS in this study

Sample	Using Tara allanite as primary RM				Data for Tera-Wasserburg plot					207Pb-corrected date (Ma)					% Conc ^c		
	n	Pb	Th	U	Th/U	238U/ 206Pb	2s	207Pb/ 206Pb	2s	f206 ^a (%)	f208 ^a (%)	206Pb/ 238U	2s	208Pb/ 232Th		2s	2s _{sys}
CAP ^b	19	184	11500	136	107	17.76	2.78	0.235	0.092	22.85	2.10	272	2	271	4	7	100
Dalibossatsu	20	9	9160	217	42	189.78	71.09	0.700	0.260	81.83	6.99	N/A	N/A	11.6	0.3	0.4	N/A
LE40010	17	1980	13900	70	200	1.96	0.15	0.193	0.028	0.51	0.13	2654	33	2610	65	83	102
LE2808	23	596	10000	211	48	5.17	0.28	0.126	0.021	6.03	1.04	1078	9	1041	44	49	104
A007	21	18	0.1	37	0.003	2.65	0.18	0.213	0.058	11.25	99.75	1866	11	N/A	N/A	N/A	N/A
A011	17	297	5160	30	177	4.48	0.80	0.178	0.129	11.80	0.57	1157	23	1190	85	88	97
A012	18	175	13100	176	77	17.24	1.54	0.124	0.098	8.81	1.15	329	4	292	21	22	113
SQ-51 G1	11	68	162	488	0.4	7.77	0.04	0.069	0.005	0.53	47.32	776	7	547	100	101	142
SQ-51 G2	12	103	155	834	0.2	8.32	0.08	0.068	0.005	0.49	34.44	728	6	629	210	210	116
Secondary reference material																	
CAP ^b	20	151	10205	103	117	18.94	0.46	0.179	0.006	15.84	1.13	277	2	276	2	6	100
Dalibossatsu [*]	33	10	11513	232	50	161.72	3.71	0.608	0.014	71.07	24.83	11	1.3	11.6	0.5	0.6	94.8

N/A, not available.

Tara allanite was used as primary reference material.

Uncertainties quoted without components related to systematic uncertainties unless otherwise stated.

Total systematic uncertainties (s_{sys}) are given at 2.0% level. Mass fraction uncertainties are ca. 20%. The individual data can be found in Table S3.

n, number of analysis.

^a f₂₀₆, common 206Pb in total 206Pb; f₂₀₆ = [(207Pb/206Pb)_{total} - (207Pb/206Pb)_{radiogenic}] / [(207Pb/206Pb)_{total} - (207Pb/206Pb)_{radiogenic}]

^b f₂₀₈, common 208Pb in total 208Pb; f₂₀₈ = [(207Pb/208Pb)_{total} - (207Pb/208Pb)_{radiogenic}] / [(207Pb/208Pb)_{total} - (207Pb/208Pb)_{radiogenic}]

^c Concordance calculated as (206Pb-238U)age / (208Pb-232Th) age * 100.

^d Samples used as secondary reference materials.

202 $\mu\text{g g}^{-1}$. For the analysed fragments, the relative standard deviation of twenty-three analyses is ca. 10% for REE and ca. 20% for U and Th (Table 4).

Allanite LE2808 contains variable common Pb with f_{206} and f_{208} ranging from 3.87 to 0.85% and 0.75 to 1.41% respectively. The dataset yielded an intercept age of 1076 ± 10 Ma (2s, MSWD = 0.7, $n = 23$; Figure 4d) by anchoring to a $^{207}\text{Pb}/^{206}\text{Pb}$ ratio of 0.91 as estimated using Stacey and Kramers' (1975) model. However, the $^{207}\text{Pb}/^{206}\text{Pb}$ model ratio of 0.91 for 1.1 Ga is considerably greater than the ordinate upper intercept of 0.54 ± 0.12 . This sample gives an intercept age of 1021 ± 34 Ma (2s, MSWD = 0.2, $n = 23$) without anchoring the upper intercept. Previous LA-ICP-MS results of LE2808 show a bimodal distribution in Tera-Wasserburg diagram and reflect a mixing between common Pb and radiogenic Pb of ca. 1100 Ma (ordinate upper intercept 0.23 ± 0.06 ; Smye *et al.* 2014). The upper intercepts obtained in both studies indicate that the initial common Pb composition of LE2808 allanite is radiogenic. The more radiogenic $^{207}\text{Pb}/^{206}\text{Pb}$ ratio can be accounted for a radiogenic common Pb source at the time of formation or some degree of alteration. Therefore, the un-anchored intercept age is more reliable in this case. The ^{207}Pb corrected weighted mean $^{206}\text{Pb}/^{238}\text{U}$ age of $1078 \pm 9/23$ Ma (2s, MSWD = 0.5, $n = 23$) is in good agreement with Smye *et al.* (2014). The final $^{208}\text{Pb}/^{232}\text{Th}$ age of $1041 \pm 44/49$ Ma (2s; MSWD = 27, $n = 23$) shows relatively large dispersion.

The mean LA-MC-ICP-MS $^{147}\text{Sm}/^{144}\text{Nd}$ and $^{143}\text{Nd}/^{144}\text{Nd}$ ratios of LE2808 are 0.1168 ± 0.0098 (2s, $n = 39$) and 0.512245 ± 0.000065 (2s, $n = 39$). The $^{147}\text{Sm}/^{144}\text{Nd}$ ratio shows a large variation with 8.40% RSD, but the calculated initial $^{143}\text{Nd}/^{144}\text{Nd}$ value shows limited variation with a mean value of 0.511402 ± 0.000042 (2s, $n = 39$). The mean $\epsilon_{\text{Nd}}(t)$ is 3.59 ± 0.83 (2s, $n = 39$). All data plot along a 1100 Ma reference isochron (Figure 3e). Two aliquots were studied using ID-MC-ICP-MS and yielded $^{147}\text{Sm}/^{144}\text{Nd}$ and $^{143}\text{Nd}/^{144}\text{Nd}$ ratios of 0.1188 ± 0.0003 (2s) and 0.512230 ± 0.0003 (2s) respectively. Laser ablation and solution-based Sm-Nd data are in good agreement with each other.

A007

Allanite A007 shows pyrite inclusions in BSE images (Figure 1f). EPMA data show that A007 is rich in REE and poor in ThO_2 . Ce_2O_3 is the most abundant REE mass fraction (8.91% m/m), followed by La_2O_3 (5.33% m/m) and Nd_2O_3 (4.81% m/m) (Table 3). LA-ICP-MS analyses demonstrate that A007 contains very little U and Th, with U ranging from 14 to 79 $\mu\text{g g}^{-1}$ and Th ranging from 0.03

to 0.44 $\mu\text{g g}^{-1}$. Chondrite-normalised REE patterns show that this sample is rich in LREE, has a strong LREE/HREE fractionation (mean $(\text{La}/\text{Lu})_{\text{N}} = 1300$) and has a strong negative Eu anomaly ($\text{Eu}/\text{Eu}^* = 0.18$).

Due to the low Th contents, ^{208}Pb is dominated by non-radiogenic Pb, and therefore, no Th-Pb age was calculated. U-Pb data define on a Tera-Wasserburg diagram a discordia with an intercept age of 1865 ± 21 Ma (2s, MSWD = 0.11, $n = 21$, Figure 6a) by anchoring to a $^{207}\text{Pb}/^{206}\text{Pb}$ ratio of 0.99 as estimated using the two-stage crustal Pb model of Stacey and Kramers (1975). A free regression of the dataset yields an upper $^{207}\text{Pb}/^{206}\text{Pb}$ ratio of 1.05 ± 0.19 and an intercept on concordia of 1878 ± 44 Ma (2s, MSWD = 0.07, $n = 21$). The upper intercept from the regression of A007 dataset agrees well with the common $^{207}\text{Pb}/^{206}\text{Pb}$ ratio for that age as estimated from the model of Stacey and Kramers (1975). A weighted mean $^{206}\text{Pb}/^{238}\text{U}$ age of $1866 \pm 11/39$ Ma (2s, MSWD = 0.1, $n = 21$) is in close agreement with the molybdenite Re-Os ages obtained for Bastnäs-type deposits (Holtstam *et al.* 2014) and also the U-Pb ages of bastnäsites from Bastnäs-type deposits (Yang *et al.* 2019).

The *in situ* $^{147}\text{Sm}/^{144}\text{Nd}$ and $^{143}\text{Nd}/^{144}\text{Nd}$ values are variable, ranging from 0.0686 to 0.1354 and from 0.511311 to 0.511867 respectively. All Sm-Nd data define an isochron age of 1884 ± 41 Ma (2s, MSWD = 4.3, $n = 65$; Figure 3f) which agrees well with the ID-TIMS U-Pb age of 1852 ± 5 Ma and the LA-ICP-MS $^{206}\text{Pb}/^{238}\text{U}$ age of 1866 ± 11 Ma, as well as the multi-mineral (e.g. bastnäsites, ferriallanite, cerite, percleveite and törebohmitite) Sm-Nd isochron from the Bastnäs deposit (1875 ± 110 Ma; Holtstam *et al.* 2014), and a bastnäsites and apatite Sm-Nd isochron from the Bastnäs deposit (1843 ± 26 Ma; Yang *et al.* 2019). The $\epsilon_{\text{Nd}}(t)$ for 1860 Ma is 1.38 ± 0.81 (2s, $n = 65$). The Solution MC-ICP-MS analysis of four separate aliquots of A007 gave similar Sm-Nd isotope compositions. Measured $^{147}\text{Sm}/^{144}\text{Nd}$ and $^{143}\text{Nd}/^{144}\text{Nd}$ ratios are 0.1106 ± 0.0021 (2s, $n = 4$) and 0.511632 ± 0.000007 (2s, $n = 4$), respectively, which gives a mean $\epsilon_{\text{Nd}}(t)$ value of 1.05 ± 0.58 . The apparently smaller variation largely reflects the larger sample size for solution MC-ICP-MS analysis, which is averaging small-scale heterogeneity.

A011

Allanite A011 shows heterogeneous domains in BSE images in addition to alterations along cracks and inclusions (Figure 1g). EPMA data show that A011 allanite contains large amount of REE, with Ce_2O_3 of 11.03% m/m , La_2O_3 of 7.06% m/m and Nd_2O_3 of 2.53% m/m (Table 3). ThO_2

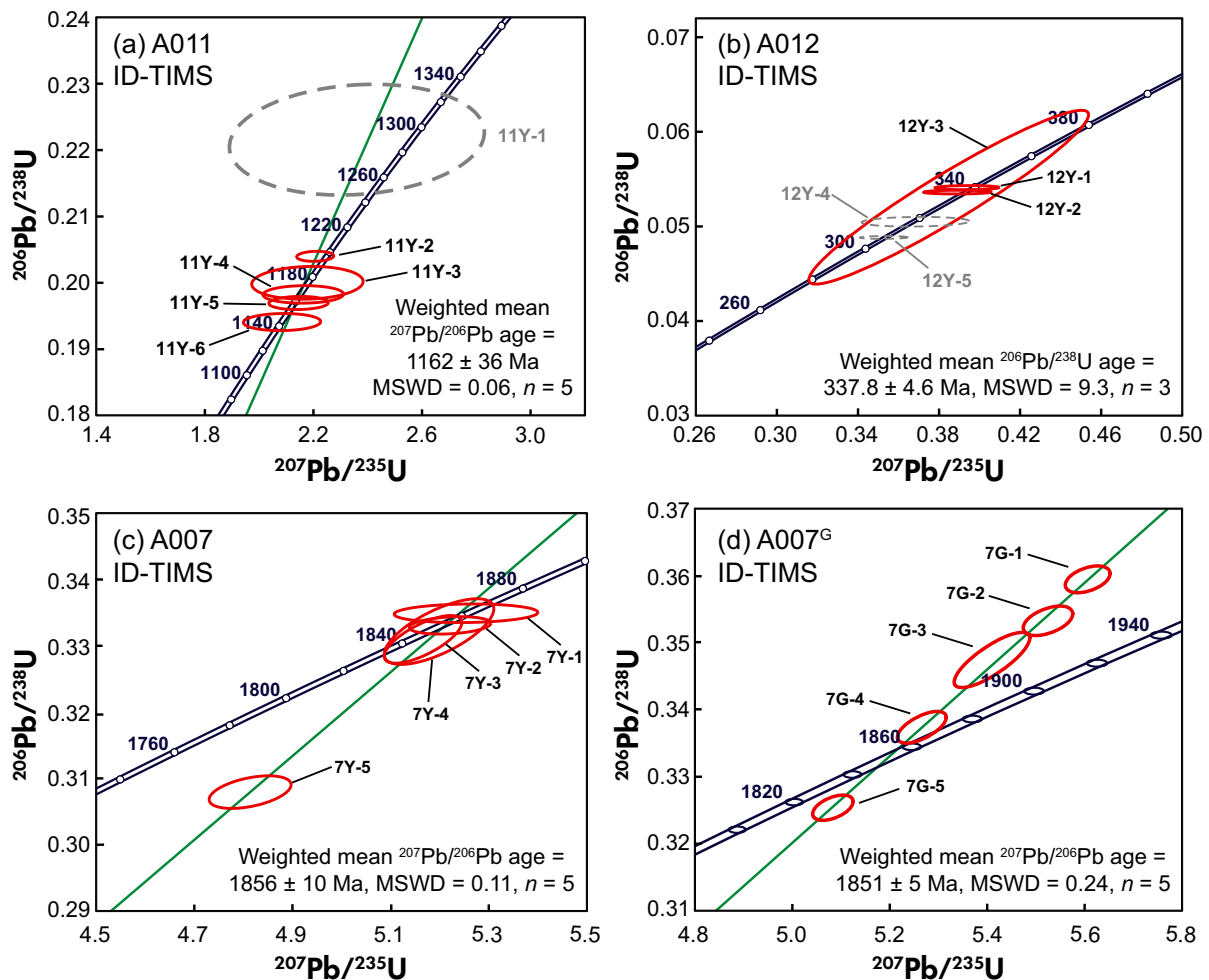


Figure 6. Concordia diagrams of ID-TIMS U-Pb results in this study. Allanite samples (a) A011, (b) A012 and (c) A007 were analysed at Jack Satterly Geochronology Laboratory, Department of Earth Sciences, University of Toronto; allanite sample (d) A007G was analysed at GFZ German Research Centre for Geosciences. Grey dashed circles in (a) and (b) were not used for age calculation. n represents the number of analyses. Ellipses in the concordia diagram represent the 95% confidence level.

mass fraction ranges from 0.30 to 0.72% m/m . REE mass fractions obtained by LA-ICP-MS exhibit strong fractionation between LREE and HREE ($(La/Lu)_N = 940$) and a strong negative Eu anomaly ($Eu/Eu^* = 0.23$). The U and Th mass fractions are variable with U ranges from 23 to 113 $\mu g\ g^{-1}$ and Th ranges from 3960 to 6820 $\mu g\ g^{-1}$.

The f_{206} and f_{208} ranges from 0.01 to 20.34% and from 0 to 1.57% respectively. The $^{208}Pb/^{232}Th$ ages show scattered distribution from 858 to 2264 Ma (Supplementary data, Table S3), which indicates the Th-Pb system of A011 allanite is disturbed. The U-Pb results for nineteen analyses are presented in a Tera-Wasserburg diagram (Figure 6b) by

forcing to an upper intercept $^{207}Pb/^{206}Pb$ ratio of 0.92, calculated from Stacey and Kramers' (1975) model. These data yield an intercept age of 1157 ± 23 Ma (2s, MSWD = 0.03, $n = 19$) and a weighted mean $^{206}Pb/^{238}U$ age of $1148 \pm 23/33$ Ma (2s, MSWD = 0.03, $n = 19$). The un-anchored data give a $^{207}Pb/^{206}Pb$ intercept of 0.90 ± 0.21 and an intercept age of 1153 ± 48 Ma (2s, MSWD = 0.03, $n = 19$). The unconstrained $^{207}Pb/^{206}Pb$ intercept agrees within uncertainty with the model $^{207}Pb/^{206}Pb$ ratio obtained from the model of Stacey and Kramers (1975). The common Pb corrected $^{208}Pb/^{232}Th$ age of $1190 \pm 85/88$ Ma (2s, MSWD = 146, $n = 19$) shows a very large dispersion.

In situ Sm-Nd data gave variable $^{147}\text{Sm}/^{144}\text{Nd}$ and $^{143}\text{Nd}/^{144}\text{Nd}$ ratios of 0.0487 ± 0.0140 (2s, $n = 55$) and 0.511691 ± 0.000115 (2s, $n = 55$), respectively, yielding a mean $\epsilon_{\text{Nd}}(t)$ value of 3.53 ± 0.78 (2s, $n = 55$). The calculated initial $^{143}\text{Nd}/^{144}\text{Nd}$ ratio shows limited variation (0.511356 ± 0.000041 , 2s, $n = 55$). Solution MC-ICP-MS analyses of four separate A011 allanite aliquots yielded $^{147}\text{Sm}/^{144}\text{Nd}$ and $^{143}\text{Nd}/^{144}\text{Nd}$ ratios of 0.0544 ± 0.0006 (2s) and 0.511718 ± 0.000013 (2s), respectively, and a mean $\epsilon_{\text{Nd}}(t)$ value of 3.20 ± 0.17 (2s). The values obtained by different methods agree within uncertainty, whereby the larger scatter for *in situ* analyses reflects the larger heterogeneity at the smaller scale.

A012

A012 allanite experienced alteration, which is visible in the BSE image (Figure 1h). The EPMA data reveal that A012 contains considerable amount of REE with Ce_2O_3 of 8.51% *m/m*, La_2O_3 of 3.83% *m/m* and Nd_2O_3 of 3.25% *m/m* and ThO_2 of 1.08% *m/m* (Table 3). Trace element determined by LA-ICP-MS indicates the large variation in REE, U and Th mass fractions. Chondrite-normalised REE patterns exhibit enrichment in LREE and a strong fractionation between LREE and HREE ($(\text{La}/\text{Lu})_{\text{N}} = 554$). A012 allanite also show a strong Eu anomaly ($\text{Eu}/\text{Eu}^* = 0.08$). The variable U and Th mass fractions range from 97 to 306 $\mu\text{g g}^{-1}$ and from 10200 to 21900 $\mu\text{g g}^{-1}$ respectively.

A012 contains considerable amount of common Pb with f_{206} and f_{208} varying from 2.45 to 22.54% and 0.31 to 3.78% respectively. A012 allanite suffers from the same problem as A011, that is its Th-Pb system was disturbed during alteration (Figure 1h). The $^{208}\text{Pb}/^{232}\text{Th}$ ages are much more scattered than the $^{206}\text{Pb}/^{238}\text{U}$ ages and range from 221.2 to 347.0 Ma (Table S3). Consequently, we only reported U-Pb age data for this sample. Eighteen analyses yielded an intercept age of 334.5 ± 4.0 Ma (2s, MSWD = 0.9, $n = 18$) by forcing to an upper intercept $^{207}\text{Pb}/^{206}\text{Pb}$ ratio of 0.86 calculated from the model of Stacey and Kramers (1975) and weighted mean $^{206}\text{Pb}/^{238}\text{U}$ age of 329.1 ± 3.7 Ma (2s, MSWD = 0.9, $n = 18$, Figure 6c). The unconstrained discordia yielded a $^{207}\text{Pb}/^{206}\text{Pb}$ ratio of 1.22 ± 0.23 , which is much higher than the model contemporaneous $^{207}\text{Pb}/^{206}\text{Pb}$ ratio of 0.86 and an intercept age of 342.1 ± 5.8 Ma (2s, MSWD = 0.02, $n = 18$). The higher $^{207}\text{Pb}/^{206}\text{Pb}$ intercept of 1.22 ± 0.23 could be accounted for by heterogeneous common Pb composition. Constrained and unconstrained intercept ages agree with each other within uncertainty and also broadly agree with the age constraints for metamorphism in this area (Rötzler and Plessen 2010, Kroner and Romer 2013).

The laser ablation Sm-Nd results of A012 allanite are presented in Table 7. The $^{147}\text{Sm}/^{144}\text{Nd}$ ratio shows large variation with a mean of 0.1093 ± 0.0195 (2s, $n = 54$), and $^{143}\text{Nd}/^{144}\text{Nd}$ ratio shows limited variation with a mean of 0.512579 ± 0.000052 (2s, $n = 54$). The calculated initial $^{143}\text{Nd}/^{144}\text{Nd}$ ratio shows limited variation (0.512239 ± 0.000035 , 2s, $n = 54$). The mean $\epsilon_{\text{Nd}}(t)$ value is 2.32 ± 1.22 (2s, $n = 54$). All $^{147}\text{Sm}/^{144}\text{Nd}$ and $^{143}\text{Nd}/^{144}\text{Nd}$ values scatter around a reference line for 340 Ma (Figure 3h). Due to large variability in Sm-Nd isotope composition and limited supply, this sample A012 was not further characterised by solution method.

SQ-51

Some grains of SQ-51 allanite exhibit distinctive alteration rims (Figure 1i). Similar to A007 allanite from a skarn-type deposit, SQ-51 allanite is enriched in U rather than Th. EPMA data show that SQ-51 contains considerable amounts of REE with Ce_2O_3 of 8.00% *m/m*, La_2O_3 of 5.39% *m/m* and Nd_2O_3 of 1.56% *m/m* (Table 3). Trace element mass fractions obtained by LA-ICP-MS show large variation. The unaltered (Group 1) and altered (Group 2) domains show no difference in LREE contents, but can be differentiated in HREE mass fractions (Figure 2i) and degree of LREE and HREE fractionation. Both domains show a weak positive Eu anomaly with $\text{Eu}/\text{Eu}^* = 2.13$. Other trace elements show little difference between the two groups of allanite.

There is a significant age difference between the two groups of allanite. Unaltered (Group 1) allanite yields an intercept age of 776.3 ± 6.9 Ma (2s, MSWD = 0.10, $n = 11$) by forcing the discordia through a $^{207}\text{Pb}/^{206}\text{Pb}$ ratio of 0.89, as estimated from the model of Stacey and Kramers (1975). The weighted mean $^{206}\text{Pb}/^{238}\text{U}$ age is 776.4 ± 7.5 Ma (2s, MSWD = 0.10, $n = 11$, Figure 6d). The unconstrained discordia for Group 1 data intercepts at a $^{207}\text{Pb}/^{206}\text{Pb}$ ratio of 4.00 ± 5.70 and an age of 779.0 ± 13 Ma (2s, MSWD = 0.02, $n = 11$). The large uncertainty of the $^{207}\text{Pb}/^{206}\text{Pb}$ intercept reflects the small spread of the data that cluster close to Concordia. Altered (Group 2) allanite yields an intercept at 728.2 ± 6.3 Ma (2s, MSWD = 0.10, $n = 12$) by forcing to a $^{207}\text{Pb}/^{206}\text{Pb}$ ratio of 0.89 estimated from the two-stage crustal Pb model of Stacey and Kramers (1975) and a weighted mean $^{206}\text{Pb}/^{238}\text{U}$ age of 728.6 ± 6.7 Ma (2s, MSWD = 0.10, $n = 12$, Figure 6d). The unconstrained discordia of the Group 2 dataset yields a $^{207}\text{Pb}/^{206}\text{Pb}$ ratio 0.78 ± 1.7 and an intercept date of 728.0 ± 12 Ma (2s, MSWD = 0.04, $n = 12$). Similarly, the dataset of Group 2 clusters is very close to the concordia, and, consequently, the $^{207}\text{Pb}/^{206}\text{Pb}$ intercept is poorly constrained.

The LA-ICP-MS U-Pb ages of altered allanite correspond well with the youngest age for granitic dykes (736 ± 7 Ma; Li *et al.* 2018) in this area.

The results of *in situ* Sm-Nd analysis are slightly variable (Figure 3i) with mean $^{147}\text{Sm}/^{144}\text{Nd}$ and $^{143}\text{Nd}/^{144}\text{Nd}$ values of 0.0408 ± 0.0043 ($2s$, $n = 62$) and 0.511538 ± 0.000067 ($2s$, $n = 62$) respectively. The calculated initial $^{143}\text{Nd}/^{144}\text{Nd}$ value shows limited variation (0.511340 ± 0.000063 , $2s$, $n = 62$) with mean $\epsilon_{\text{Nd}}(t)$ value of -6.72 ± 1.24 ($2s$, $n = 62$). Unaltered and altered SQ-51 allanite show no difference in their Sm-Nd isotope systematics. Because of the limited availability of sample material, the Sm-Nd isotope systematics of SQ-51 allanite was not analysed using the solution method.

U-Pb ID-TIMS geochronology

Three allanite samples (A007, A011 and A012) were selected for U-Pb ID-TIMS analysis due to their relatively homogeneous ages and lower common Pb contents.

Six fractions of A011 allanite were analysed. The common Pb contents and Th/U ratios range from 2.1 to $4.7 \mu\text{g g}^{-1}$ and 173.1 to 213.5 respectively. On a Wetherill diagram, all data obtained from fragments of A011 allanite fall on the concordia with $^{206}\text{Pb}/^{238}\text{U}$ ages between 1143 and 1289 Ma (Table 6; Figure 7a). The significant scatter is mainly due to samples with measured low $^{206}\text{Pb}/^{204}\text{Pb}$ values (67.4–173.8; Table 6). Fraction 11Y-1, with low measured $^{206}\text{Pb}/^{204}\text{Pb}$ ratios, has a larger analytical uncertainty than other fractions and, thus, was not used for age calculation. Five aliquots constrain a weighted mean $^{207}\text{Pb}/^{206}\text{Pb}$ age of 1162 ± 36 Ma ($2s$, MSWD = 0.06). This age agrees well with the LA-ICP-MS results and the published zircon U-Pb ID-TIMS age (Barth *et al.* 1995), but disagrees with an earlier reported allanite Th-Pb age (1006 ± 37 Ma; Catlos *et al.* 2000). This age difference may be caused by open system behaviour of the U-Th-Pb system or late hydrothermal alteration (Figure 1g). The cause of the age deviation remains enigmatic as the measurement data have not been published (Catlos *et al.* 2000). It is most likely related to the relatively high Th contents that cause metamictisation, which facilitates Pb redistribution during later hydrothermal alteration (Figure 1g). The relatively high amount of common Pb in this sample increases the uncertainty of the correction of initially present Pb.

Five fractions of A012 allanite were analysed. The Pb isotopic composition of the individual fractions is relatively radiogenic with a $^{206}\text{Pb}/^{204}\text{Pb}$ range of 218.1–430.9 (Table 6). Common Pb ranged from 0.8 to $3.2 \mu\text{g g}^{-1}$ and

Th/U ranged from 43.7 to 56.5. On a Wetherill diagram, all A012 allanite analyses are concordant, but do not overlap within analytical uncertainty. The $^{206}\text{Pb}/^{238}\text{U}$ ages of measured fractions fall between 339 and 307 Ma (Table 6; Figure 7b). Fractions 12Y-4 and 12Y-5 yield lower apparent $^{206}\text{Pb}/^{238}\text{U}$ ages than the other fractions, which may be caused by alteration (Figure 1h), and were not used for age calculation. Three fractions of A012 sample (one with a very large uncertainty) give a weighted mean $^{206}\text{Pb}/^{238}\text{U}$ age of 337.8 ± 4.6 Ma ($2s$, MSWD = 9.3). This value agrees with our LA-ICP-MS results and previously reported age data of this region (Kroner and Romer 2013).

Sample A007 was analysed in two different laboratories using ID-TIMS. The data shown in Figure 7c were obtained at University of Toronto. Four of the five analysed fragments are concordant, and one fraction is slightly discordant possibly due to Pb-loss. Apparent $^{206}\text{Pb}/^{238}\text{U}$ ages range from 1730 to 1862 Ma (Table 6; Figure 7c). All analyses define a Pb-loss isochron line with an upper intercept age of 1856 ± 12 Ma ($2s$, MSWD = 0.14) and weighted mean $^{207}\text{Pb}/^{206}\text{Pb}$ age of 1856 ± 11 Ma ($2s$, MSWD = 0.14). The data shown in Figure 7d were obtained at GFZ. Five fractions were analysed, and all analyses define a discordia with an upper intercept age of 1852 ± 7 Ma ($2s$, MSWD = 0.29) and weighted mean $^{207}\text{Pb}/^{206}\text{Pb}$ age of 1851 ± 5 Ma ($2s$, MSWD = 0.24). The ID-TIMS results from two different laboratories agree with each other within uncertainty. For an old sample like A007, the $^{207}\text{Pb}/^{206}\text{Pb}$ age is generally considered more reliable than the $^{206}\text{Pb}/^{238}\text{U}$ age (Mattinson 1987). The results from the two laboratories yield a weighted mean $^{207}\text{Pb}/^{206}\text{Pb}$ age of 1852 ± 5 Ma ($2s$, MSWD = 0.21).

Discussion

Evaluation of potential allanite reference materials for *in situ* U-Th-Pb dating

The LA-ICP-MS U-Th-Pb analytical data of the investigated allanite samples are summarised in Table 5. Tara allanite comprises minimal internal zoning and small mineral inclusions, which is characterised by relatively low mass fractions of Pb ($139\text{--}312 \mu\text{g g}^{-1}$) and U ($39\text{--}94 \mu\text{g g}^{-1}$), high mass fraction of Th ($7460\text{--}18300 \mu\text{g g}^{-1}$) and variable Th/U ($139\text{--}263$). Tara allanite is the most widely used reference material for U-Th-Pb dating (Gregory *et al.* 2007, Korh 2014, Smye *et al.* 2014, Liao *et al.* 2020), due to its relatively low common Pb composition (Figure 5b). Nonetheless, Tara allanite is, however, not isotopically homogeneous at the fine-scale (Smye *et al.* 2014), and Burn *et al.* (2017) argued that no U-Pb reference value can be provided. In this study,

Table 6.
ID-TIMS U-Pb measurement results for studied allanite fragments

Sample	Mass (mg)	U ($\mu\text{g g}^{-1}$)	Th/U	Pb _c ($\mu\text{g g}^{-1}$)	Measured $^{206}\text{Pb}/^{204}\text{Pb}$	$^{207}\text{Pb}/^{235}\text{U}$	2s	$^{206}\text{Pb}/^{238}\text{U}$	2s	Rho	$^{207}\text{Pb}/^{206}\text{Pb}$	2s	Age (Ma)					
													$^{206}\text{Pb}/^{238}\text{U}$	2s	$^{207}\text{Pb}/^{235}\text{U}$	2s		
A007 (Bergslagen, Sweden)																		
7Y-1	0.010	22	0.06	2.5	188.6	5.2540	0.1195	0.33483	0.00116	0.10	0.1138	0.0026	1862	6	1861	19	1861	41
7Y-2	0.010	26	0.05	2.4	225.2	5.2214	0.0678	0.33299	0.00109	0.25	0.1137	0.0014	1853	5	1856	11	1860	23
7Y-3	0.021	31	0.03	2.8	228.8	5.1991	0.0914	0.33206	0.00406	0.69	0.1136	0.0014	1848	20	1852	15	1857	23
7Y-4	0.019	36	0.10	2.2	324.9	5.1662	0.0645	0.33088	0.00293	0.71	0.1132	0.0010	1843	14	1847	11	1852	16
7Y-5	0.025	27	0.02	2.2	229.4	4.8138	0.0682	0.30783	0.00199	0.45	0.1134	0.0014	1730	10	1787	12	1855	23
A011 (southern California, USA)																		
11Y-1	0.026	17	179.8	4.6	67.4	2.3550	0.3816	0.22135	0.00676	0.15	0.0772	0.0123	1289	36	1229	119	1125	337
11Y-2	0.017	50	179.5	3.9	173.8	2.2062	0.0558	0.20386	0.00059	0.10	0.0785	0.0020	1196	3	1183	18	1159	50
11Y-3	0.025	27	176.2	3.2	118.8	2.1773	0.1684	0.19986	0.00203	0.08	0.0790	0.0061	1175	11	1174	55	1172	157
11Y-4	0.017	54	173.1	4.7	155.9	2.1630	0.1216	0.19811	0.00108	0.06	0.0792	0.0044	1165	6	1169	39	1177	113
11Y-5	0.016	16	213.5	2.1	109.5	2.1448	0.0899	0.19686	0.00081	0.04	0.0790	0.0033	1159	4	1163	29	1173	84
11Y-6	0.017	18	N/A	3.0	87.5	2.0839	0.1165	0.19395	0.00105	0.05	0.0779	0.0044	1143	6	1144	39	1145	113
A012 (Großhartmannsdorf, Saxony, Germany)																		
12Y-1	0.010	79	53.1	0.8	339.6	0.3940	0.0130	0.05405	0.00016	0.09	0.0529	0.0017	339.4	1.0	337	10	323	76
12Y-2	0.005	253	56.5	2.8	333.0	0.3891	0.0138	0.05356	0.00016	0.07	0.0527	0.0019	336.3	1.0	334	10	315	82
12Y-3	0.024	229	55.9	2.3	356.6	0.3860	0.0573	0.05322	0.00771	0.97	0.0526	0.0018	334.2	47.2	331	42	312	80
12Y-4	0.024	203	47.6	3.2	218.1	0.3683	0.0217	0.05043	0.00041	0.12	0.0530	0.0031	317.2	2.5	318	16	328	136
12Y-5	0.013	225	43.7	1.6	430.9	0.3528	0.0097	0.04876	0.00012	0.08	0.0525	0.0014	306.9	0.7	307	7	306	63
A007^c (Bergslagen, Sweden)																		
7G-1	0.211	28	0.07	3.3	192.5	5.6062	0.0376	0.35946	0.00163	0.43	0.1131	0.0007	1980	8	1917	6	1850	11
7G-2	0.178	22	0.06	2.6	184.7	5.5248	0.0415	0.035327	0.00179	0.48	0.1134	0.0008	1950	9	1905	6	1855	12
7G-3	0.283	25	0.11	2.9	189.2	5.4098	0.0635	0.034742	0.00337	0.80	0.1129	0.0008	1886	16	1886	10	1847	13
7G-4	0.361	34	0.11	3.5	207.0	5.2657	0.0410	0.033738	0.00193	0.63	0.1132	0.0007	1863	9	1863	7	1851	11
7G-5	0.318	31	0.13	3.2	198.7	5.0833	0.0340	0.032538	0.00154	0.49	0.1133	0.0007	1833	6	1833	6	1853	11

Italicised lines not included in age calculation. N/A, not available.

Th/U calculated from radiogenic $^{208}\text{Pb}/^{206}\text{Pb}$ ratio and $^{207}\text{Pb}/^{206}\text{Pb}$ age assuming concordance.

Pb_c is total common Pb. Total blanks were less than 1 pg for lead and less than 0.1 pg for uranium at University of Toronto. Total blanks were less than 1.5 pg for lead and less than 1 pg for uranium at GFZ German Research Centre for Geosciences.

Pb/U ratios corrected for fractionation, common Pb in the spike, initial common Pb and blank. All uncertainties were estimated using a Monte-Carlo simulation with the following uncertainties: measurement uncertainties, 30% uncertainty for the correction of mass fractionation, 50% uncertainty of the amount of blank Pb and U, 0.5, 0.1, and 0.5 absolute uncertainty for $^{206}\text{Pb}/^{204}\text{Pb}$, $^{207}\text{Pb}/^{204}\text{Pb}$ and $^{208}\text{Pb}/^{204}\text{Pb}$ of the blank and initial Pb composition respectively. Correction for ^{230}Th disequilibrium in $^{206}\text{Pb}/^{238}\text{U}$ and $^{207}\text{Pb}/^{235}\text{U}$ assuming Th/U of 4.2 in the magma.

Rho is the correlation coefficients of $^{206}\text{Pb}/^{238}\text{U}$ and $^{207}\text{Pb}/^{235}\text{U}$ uncertainties on the concordia plot.

Decay constants are those of Jaffey et al. (1971); ^{238}U and ^{235}U are $1.55125 \times 10^{-10} \text{ y}^{-1}$ and $9.8485 \times 10^{-10} \text{ y}^{-1}$.

$^{238}\text{U}/^{235}\text{U}$ ratio of 137.818 (Hess et al. 2012) used for $^{207}\text{Pb}/^{206}\text{Pb}$ model age calculations.

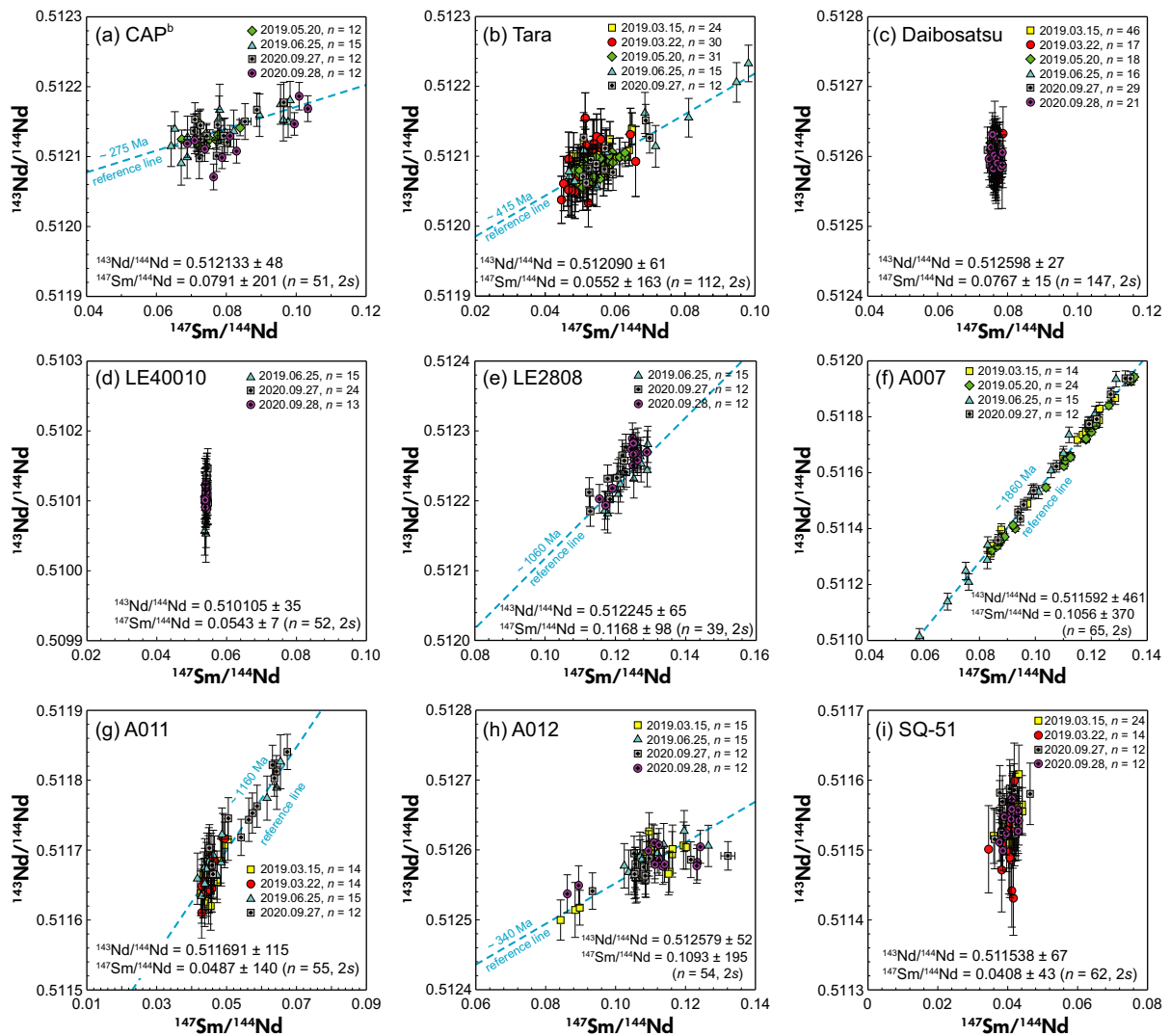


Figure 7. Diagrams of $^{147}\text{Sm}/^{144}\text{Nd}$ - $^{143}\text{Nd}/^{144}\text{Nd}$ isotope ratios for the studied allanite samples. (a) CAPb, (b) Tara, (c) Daibosatsu, (d) LE40010, (e) LE2808, (f) A007, (g) A011, (h) A012 and (i) SQ-51. *n* represents the number of analyses.

Tara allanite was used as primary reference materials using the ratios $^{206}\text{Pb}/^{238}\text{U} = 0.0651 \pm 0.0013$, $^{207}\text{Pb}/^{235}\text{U} = 0.7920 \pm 0.0390$ and $^{208}\text{Pb}/^{232}\text{Th} = 0.0207 \pm 0.0004$ from previous studies (Smye *et al.* 2014, Burn *et al.* 2017). This sample contains variable amount of common Pb; therefore, some analyses had to be rejected during the analysis. CAPb is another well-studied allanite. It has experienced some degree of alteration. It is characterised by relatively low mass fractions of Pb (146–327 $\mu\text{g g}^{-1}$) and U (58–245 $\mu\text{g g}^{-1}$), high mass fraction of Th (8510–15600 $\mu\text{g g}^{-1}$) and variable Th/U (39–151). It has relatively radiogenic Pb isotopic compositions with $f_{206} = 22.85\%$ and $f_{208} = 2.10\%$, and concordance between U-Pb and Th-Pb systems. Therefore, CAPb is a good candidate to be a primary reference material for Th-Pb dating and a secondary reference material for U-Pb dating for LA-ICP-

MS analysis. However, CAPb awaits a full investigation by ID-TIMS. Daibosatsu allanite is characterised with a fairly homogenous chemical composition with Pb of 17 to 21 $\mu\text{g g}^{-1}$, U of 37 to 45 $\mu\text{g g}^{-1}$ and Th of 8040 to 9580 $\mu\text{g g}^{-1}$. The Daibosatsu allanite is not an ideal candidate for a primary reference material for U-Th-Pb dating, despite the fact that LA-ICP-MS and SIMS $^{208}\text{Pb}/^{232}\text{Th}$ ages are identical within analytical uncertainty (Liao *et al.* 2020). Major problems with Daibosatsu allanite result from the extremely high proportion of common Pb ($f_{206} = 81.83\%$, and $f_{208} = 6.99\%$) and the need to correct the excess ^{206}Pb derived from the decay of excess ^{230}Th , which results in the discordance in U-Pb and Th-Pb systems. Daibosatsu allanite, however, may serve as a secondary reference material to be used in quality control of Cenozoic samples. LE40010 allanite

is characterised by homogeneous chemical mass fractions of Pb (1897–2100 $\mu\text{g g}^{-1}$), U (67–73 $\mu\text{g g}^{-1}$) and Th (13200–14500 $\mu\text{g g}^{-1}$), and also a narrow range of Th/U ratios of 195–206. LE40010 allanite has the lowest contribution of common Pb (f_{206} and f_{208} are below 1%). The weighted mean $^{206}\text{Pb}/^{238}\text{U}$ age of $2654 \pm 33/63$ Ma (2s, MSWD = 0.8, $n = 17$, Table 5) is well defined; the weighted mean $^{208}\text{Pb}/^{232}\text{Th}$ ages show larger dispersion ($2610 \pm 65/83$ Ma, 2s, MSWD = 15, $n = 17$, Table 5). However, the obtained U-Pb and Th-Pb ages agree well with each other, meaning that this allanite can be used as a primary reference material for U-Pb dating (Smye *et al.* 2014). Although there is some scatter in the Th/U ratios, the concordance with the U-Pb system means the material is suitable to be used as a primary reference material for U-Pb dating and a secondary reference material for Th-Pb dating. As for sample LE2808, this sample is characterised by low mass fractions of Pb (496–704 $\mu\text{g g}^{-1}$) and U (161–249 $\mu\text{g g}^{-1}$), and high mass fractions of Th (7850–12400 $\mu\text{g g}^{-1}$). Th/U ratio ranges from 43 to 61. Only the unaltered and inclusion-free domains were analysed as identified with BSE image analysis, which improved the reliability of the age data. Even though the $^{206}\text{Pb}/^{238}\text{U}$ and $^{208}\text{Pb}/^{232}\text{Th}$ ages coincide within uncertainty, the $^{208}\text{Pb}/^{232}\text{Th}$ age exhibits large dispersion. LE2808 is not suitable to be a primary reference material for Th-Pb dating, but may serve as secondary U-Pb dating reference material for LA-ICP-MS analysis.

Allanite samples A007, A011, A012 and SQ-51 are only reported in this study. A007 allanite is characterised with very low mass fraction of Th varying from 0.001 to 0.016 $\mu\text{g g}^{-1}$. Lead and U mass fractions are variable with Pb of 10–44 $\mu\text{g g}^{-1}$ and U 14–79 $\mu\text{g g}^{-1}$ respectively. The suitability of A007 allanite as a primary U-Pb reference material is compromised by the variable and relatively high common Pb contents (f_{206} ranging from 6.66% to 19.02%). Allanite A007 shows very good reproducibility (with $^{206}\text{Pb}/^{238}\text{U}$ age ranging from 1874 to 1847 Ma), and the *in situ* U-Pb age (1865 ± 21 Ma) agrees well with the ID-TIMS ages (1856 ± 10 Ma from JSGL; 1851 ± 4 Ma from GFZ) produced by two laboratories. Sample A011 is characterised by variable mass fractions of Pb (235–412 $\mu\text{g g}^{-1}$), U (23–113 $\mu\text{g g}^{-1}$) and Th (3960–6280 $\mu\text{g g}^{-1}$). The measured U-Pb ages of allanite A011 have a limited dispersion, and the LA-ICP-MS age (1157 ± 23 , MSWD = 0.63, $n = 19$) is consistent with the ID-TIMS age (1162 ± 36 , MSWD = 0.06, $n = 5$). In contrast, the Th-Pb system shows considerable scatter ($^{208}\text{Pb}/^{232}\text{Th}$ age of $1190 \pm 85/88$ Ma, 2s, MSWD = 146, $n = 19$), but the U-Pb and Th-Pb systems are essentially concordant. Accordingly, allanite A011 may be used as a secondary reference material for U-Pb dating, since it has variable amounts of common Pb (f_{206} ranging from

3.87% to 8.85%), provided BSE images are used to avoid altered sections and inclusions. Sample A012 is characterised by large variation in Pb (153–216 $\mu\text{g g}^{-1}$), U (97–111 $\mu\text{g g}^{-1}$) and Th (10200–21900 $\mu\text{g g}^{-1}$) mass fractions. Allanite A012 shows (similar to allanite A011) limited dispersion in $^{206}\text{Pb}/^{238}\text{U}$ ages, but large dispersion in $^{208}\text{Pb}/^{232}\text{Th}$ ages ($292 \pm 21/22$ Ma, 2s, MSWD = 121, $n = 18$), which along with heterogeneous contributions of common Pb, makes allanite A012 unsuitable as a primary reference material. The $^{208}\text{Pb}/^{232}\text{Th}$ ages measured by LA-ICP-MS are not in agreement with the U-Pb ages. This discordance might be the result of hydrothermal alteration, which is obvious in BSE image (Figure 1h). Allanite A012, however, could be a suitable secondary reference material for U-Pb dating. Allanite SQ-51 exhibits a conspicuous age heterogeneity and, therefore, is not suitable to serve as a reference material. The discordance between U-Pb and Th-Pb systems might also be accounted for the hydrothermal alteration identified in the BSE image (Figure 1i).

In summary, allanite LE40010 has potential as a primary reference material for U-Pb dating but requires additional ID-TIMS data, and allanite CAP^b is a good primary reference material for Th-Pb dating but also needs additional ID-TIMS data. Allanite samples CAP^b, LE2808, A007, A011 and A012 are suited to serve as secondary reference material for U-Pb dating. LE40010 would be suitable as a secondary reference material for Th-Pb dating. Daibosatsu can serve as a secondary reference material for U-Pb or Th-Pb dating of Cenozoic samples, although low sensitivity instrumentation may be hampered with low counts on this young material for U-Pb. SQ-51 is not appropriate to serve as reference material due to age heterogeneity. As highlighted by previous studies, the existence of inclusions and alteration of some grains means that it is preferable to characterise individual grains before using them as a reference material. We also reiterate two points: (1) ‘reference ages’ should not be used for U-Th-Pb dating, but normalisation of individual Pb/U and Pb/Th ratios should use individually measured ratios as determined by ID-TIMS (Horstwood *et al.* 2016), or at least cross-calibrated with materials that have ID-TIMS values; (2) the uncertainty of the reference material U/Pb and/or Th/Pb ratios, should be propagated into the final age uncertainty, as this limits our ability to ‘know’ what the age of the sample is (Horstwood *et al.* 2016), that is we cannot know our samples to a better precision than our reference materials.

Potential of allanite for *in situ* Sm-Nd isotope measurement

Sm-Nd isotopic results of allanite samples investigated here are summarised in Tables 7 and 8. All measured

Table 7.
Sm-Nd isotopic data for allanite obtained by LA-MC-ICP-MS in this study

Allanite	n	$[\frac{147}{144}\text{Sm}/\frac{144}{144}\text{Nd}]_{\text{m}}$	2s	2s _{sys}	2RSD (%)	$[\frac{143}{144}\text{Nd}/\frac{144}{144}\text{Nd}]_{\text{m}}$	2s	2s _{sys}	$[\frac{143}{144}\text{Nd}/\frac{144}{144}\text{Nd}]_{\text{t}}$	2s	$[\frac{145}{144}\text{Nd}/\frac{144}{144}\text{Nd}]_{\text{m}}$	2s	$\epsilon_{\text{Nd}}(t)$	2s
CAP^b (~ 275 Ma)														
2019.05.20	12	0.0751	0.0084	0.0084	11.21	0.512127	0.000020	0.000055	0.511992	0.000020	N/A	N/A	-5.70	0.39
2019.06.25	15	0.0801	0.0251	0.0251	31.32	0.512140	0.000053	0.000074	0.511996	0.000035	0.348387	0.000028	-5.62	0.69
2020.09.27	12	0.0782	0.0164	0.0164	21.02	0.512138	0.000047	0.000070	0.511998	0.000037	0.348395	0.000019	-5.59	0.72
2020.09.28	12	0.0827	0.0238	0.0238	28.77	0.512126	0.000061	0.000080	0.511977	0.000041	0.348387	0.000014	-6.00	0.79
Mean	51	0.0791	0.0201	0.0201	25.46	0.512133	0.000048	0.000070	0.511991	0.000037	0.348390	0.000023	-5.72	0.72
Tara (~ 415 Ma)														
2019.03.15	24	0.0537	0.0102	0.0102	18.95	0.512088	0.000046	0.000069	0.511942	0.000036	0.348389	0.000019	-3.19	0.69
2019.03.22	30	0.0525	0.0102	0.0102	19.47	0.512095	0.000061	0.000080	0.511952	0.000052	0.348381	0.000034	-2.96	1.01
2019.05.20	31	0.0552	0.0078	0.0078	14.14	0.512085	0.000028	0.000058	0.511935	0.000022	N/A	N/A	-3.28	0.43
2019.06.25	15	0.0619	0.0342	0.0342	55.26	0.512110	0.000109	0.000120	0.511942	0.000038	0.348390	0.000029	-3.16	0.74
2020.09.27	12	0.0568	0.0129	0.0129	22.65	0.512097	0.000054	0.000074	0.511942	0.000040	0.348395	0.000019	-3.14	0.78
Mean	112	0.0552	0.0163	0.0163	29.49	0.512090	0.000061	0.000080	0.511940	0.000038	0.348387	0.000029	-3.18	0.75
Dalbosatsu (~ 13 Ma)														
2019.03.15	46	0.0767	0.0011	0.0011	1.46	0.512599	0.000023	0.000056	0.512592	0.000023	0.348389	0.000015	-0.56	0.45
2019.03.22	17	0.0767	0.0007	0.0007	0.87	0.512599	0.000038	0.000064	0.512592	0.000038	0.348380	0.000030	-0.56	0.74
2019.05.20	18	0.0767	0.0010	0.0010	1.25	0.512599	0.000026	0.000057	0.512592	0.000026	N/A	N/A	-0.56	0.51
2019.06.25	16	0.0767	0.0016	0.0016	2.11	0.512599	0.000027	0.000058	0.512592	0.000027	0.348387	0.000029	-0.56	0.53
2020.09.27	29	0.0767	0.0019	0.0019	2.54	0.512599	0.000027	0.000058	0.512592	0.000027	0.348394	0.000024	-0.56	0.52
2020.09.28	21	0.0767	0.0023	0.0023	3.00	0.512599	0.000027	0.000058	0.512592	0.000027	0.348395	0.000014	-0.57	0.52
Mean	147	0.0767	0.0015	0.0015	1.97	0.512598	0.000027	0.000058	0.512591	0.000027	0.348390	0.000024	-0.58	0.53
LE2808 (~ 1100 Ma)														
2019.06.25	15	0.1141	0.0083	0.0083	7.26	0.512241	0.000062	0.000080	0.511417	0.000030	0.348388	0.000022	3.89	0.59
2020.09.27	12	0.1162	0.0084	0.0084	7.21	0.512242	0.000060	0.000079	0.511404	0.000030	0.348396	0.000015	3.63	0.59
2020.09.28	12	0.1209	0.0076	0.0076	6.31	0.512254	0.000063	0.000081	0.511380	0.000029	0.348390	0.000015	3.18	0.57
Mean	39	0.1168	0.0098	0.0098	8.40	0.512245	0.000065	0.000083	0.511402	0.000042	0.348391	0.000019	3.59	0.83
LE40010 (~ 2800 Ma)														
2019.06.25	15	0.0539	0.0004	0.0004	0.71	0.510099	0.000047	0.000069	0.509103	0.000047	0.348390	0.000047	1.96	0.92
2020.09.27	24	0.0546	0.0004	0.0004	0.82	0.510112	0.000030	0.000059	0.509104	0.000030	0.348393	0.000021	1.99	0.59
2020.09.28	13	0.0541	0.0003	0.0003	0.63	0.510100	0.000020	0.000055	0.509100	0.000022	0.348393	0.000014	1.90	0.43
Mean	52	0.0543	0.0007	0.0007	1.28	0.510105	0.000035	0.000062	0.509103	0.000034	0.348392	0.000024	1.96	0.66
A007 (~ 1860 Ma)														
2019.03.15	14	0.1058	0.0341	0.0341	32.25	0.511597	0.000422	0.000425	0.510302	0.000024	0.348390	0.000019	1.48	0.47
2019.05.20	24	0.1090	0.0333	0.0333	30.6	0.511618	0.000412	0.000415	0.510284	0.000018	N/A	N/A	1.05	0.35
2019.06.25	15	0.0957	0.0437	0.0437	45.62	0.511487	0.000567	0.000569	0.510315	0.000051	0.348393	0.000019	1.73	0.99
2020.09.27	12	0.1109	0.0329	0.0329	29.71	0.511667	0.000415	0.000418	0.510310	0.000029	0.348395	0.000019	1.55	0.56

Table 7 (continued).
Sm-Nd isotopic data for allanite obtained by LA-MC-ICP-MS in this study

Allanite	n	$^{147}\text{Sm}/^{144}\text{Nd}$	2s	2s _{sys}	2RSD (%)	$^{143}\text{Nd}/^{144}\text{Nd}$	2s	2s _{sys}	$^{143}\text{Nd}/^{144}\text{Nd}(t)$	2s	$^{145}\text{Nd}/^{144}\text{Nd}$	2s	$\epsilon_{\text{Nd}}(t)$	2s
Mean	65	0.1056	0.0370	0.0370	35.04	0.511592	0.000461	0.000464	0.510300	0.000040	0.348392	0.000018	1.38	0.81
A011 (~ 1160 Ma)														
201903.15	14	0.0456	0.0048	0.0048	10.42	0.511656	0.000060	0.000079	0.511308	0.000040	0.348389	0.000024	3.29	0.79
201903.22	14	0.0453	0.0042	0.0042	9.17	0.511675	0.000063	0.000081	0.511322	0.000040	0.348381	0.000024	3.71	0.78
201906.25	15	0.0489	0.0160	0.0160	32.66	0.511698	0.000111	0.000122	0.511326	0.000036	0.348393	0.000028	3.64	0.70
202009.27	12	0.0562	0.0155	0.0155	27.65	0.511754	0.000114	0.000125	0.511326	0.000036	0.348392	0.000011	3.64	0.74
Mean	55	0.0487	0.0140	0.0140	28.83	0.511691	0.000115	0.000126	0.511356	0.000041	0.348388	0.000025	3.53	0.78
A012 (~ 335 Ma)														
201903.15	15	0.1081	0.0228	0.0228	21.10	0.512579	0.000077	0.000093	0.512342	0.000043	0.348382	0.000021	2.63	0.84
201906.25	15	0.1092	0.0131	0.0131	11.99	0.512582	0.000040	0.000065	0.512343	0.000024	0.348393	0.000019	2.66	0.48
202009.27	12	0.1095	0.0188	0.0188	17.18	0.512572	0.000033	0.000061	0.512332	0.000033	0.348397	0.000019	2.45	0.65
202009.27	12	0.1110	0.0239	0.0239	21.50	0.512582	0.000044	0.000068	0.512339	0.000038	0.348395	0.000018	2.58	0.74
Mean	54	0.1093	0.0195	0.0195	17.75	0.512579	0.000052	0.000073	0.512339	0.000035	0.348391	0.000021	2.59	0.69
SQ-51 (~ 740 Ma)														
201903.15	24	0.0412	0.0038	0.0038	9.33	0.511545	0.000044	0.000067	0.511345	0.000037	0.348396	0.000031	-6.71	0.72
201903.22	14	0.0403	0.0040	0.0040	10.04	0.511517	0.000089	0.000103	0.511321	0.000088	0.348391	0.000048	-7.16	1.71
202009.27	12	0.0406	0.0058	0.0058	14.19	0.511556	0.000057	0.000077	0.511359	0.000059	0.348390	0.000022	-6.34	1.15
202009.28	12	0.0410	0.0037	0.0037	9.07	0.511541	0.000037	0.000063	0.511342	0.000036	0.348394	0.000020	-6.67	0.71
Mean	62	0.0408	0.0043	0.0043	10.46	0.511538	0.000067	0.000084	0.511340	0.000063	0.348393	0.000032	-6.72	1.24

N/A, not available; RSD, relative standard deviation.

Total systematic uncertainties (ϵ_{sys}) for $^{147}\text{Sm}/^{144}\text{Nd}$ and $^{143}\text{Nd}/^{144}\text{Nd}$ ratios are given at 0.02% level.

$\epsilon_{\text{Nd}}(t)$ was calculated as an initial value with the age obtained by U-Pb dating of allanite in this study.

$\lambda^{147}\text{Sm} = 6.54 \times 10^{-10} \text{ y}^{-1}$ (Lugmair and Marti 1978); $(^{147}\text{Sm}/^{144}\text{Nd})_{\text{CHUR}} = 0.1967$; $(^{143}\text{Nd}/^{144}\text{Nd})_{\text{CHUR}} = 0.512638$ (Jacobsen and Wasserburg 1980)

The Daibosatsu allanite was used as primary reference material, and the Tara allanite was used for data monitoring. The complete dataset can be found in Table S4.

n, number of analyses.

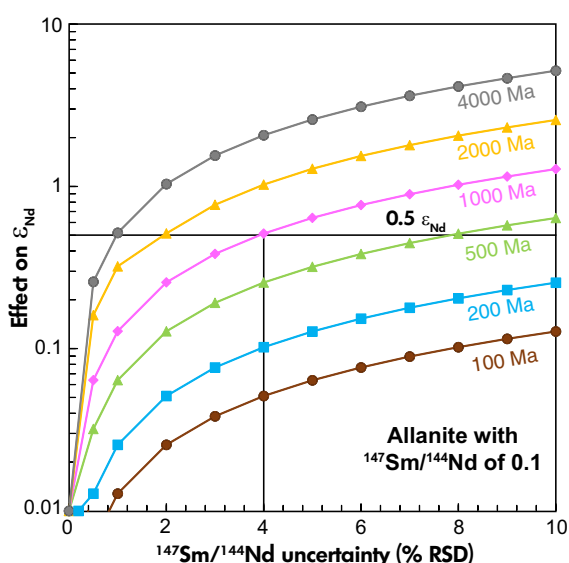


Figure 8. Effects on $\epsilon_{Nd}(0)$ of radiogenic in-growth ^{143}Nd in allanite crystals with variable crystallisation age and a $^{147}Sm/^{144}Nd$ ratio of 0.1. The maximum uncertainty of the $^{147}Sm/^{144}Nd$ ratio to achieve a precision of 0.5ϵ for the initial Nd isotopic composition depends on the age of the samples. For a 1000 Ma old sample, the uncertainty of the $^{147}Sm/^{144}Nd$ ratio should be less than 4%.

$^{147}Sm/^{144}Nd$ and $^{143}Nd/^{144}Nd$ ratios for Daibosatsu allanite show very limited variation. Especially, the RSD of all measured $^{147}Sm/^{144}Nd$ ratios are less than 2% (Table 7) on average, indicating the homogeneity of Sm-Nd isotopic composition for Daibosatsu allanite.

Previous *in situ* allanite Sm-Nd isotope analyses mainly used NIST SRM 610, synthetic JNdi glass and LREE glass for calibration and standardisation (McFarlane and McCulloch 2007, 2008, Fisher *et al.* 2011, Hammerli *et al.* 2014). As noted by McFarlane and McCulloch (2008), the suitability of NIST SRM 610 as reference material is compromised by the evidently different ablation behaviour between NIST SRM 610 and allanite. Fisher *et al.* (2011) and Hammerli *et al.* (2014) indicate that the JNdi glass and LREE glasses can be used as reference materials to calibrate younger allanite samples, since the accuracy of the measured $^{147}Sm/^{144}Nd$ ratio is less important than for old samples (see Figure 8). However, the use of a matrix-matched reference material is critical to obtain precise and accurate $^{147}Sm/^{144}Nd$ ratios, especially for ancient samples (Foster and Vance 2006, Fisher *et al.* 2011, Iizuka *et al.* 2011, Liu *et al.* 2012). The initial $^{143}Nd/^{144}Nd$ ratios and $\epsilon_{Nd}(t)$ values are calculated using the measured $^{147}Sm/^{144}Nd$ and $^{143}Nd/^{144}Nd$ ratios and the age of the mineral. Thus, the precise and accurate

measurement on $^{147}Sm/^{144}Nd$ is critical, especially for ancient allanite. For a ca. 1.0 Ga allanite sample with $^{147}Sm/^{144}Nd$ of 0.1, the analytical uncertainty of the $^{147}Sm/^{144}Nd$ ratio has to be less than 4% to achieve an uncertainty of $< 0.5\epsilon_{Nd}$ for the initial $^{143}Nd/^{144}Nd$ (Figure 8). In this work, problems associated with laser-induced fractionation of $^{147}Sm/^{144}Nd$ and instrumental drift are reduced using Daibosatsu allanite as a matrix-matched natural reference material. Although the limited variation of $^{147}Sm/^{144}Nd$ is vital for a primary reference material, it is not necessarily indispensable for a secondary reference material. The crystallisation of allanite depletes the source reservoir in LREE, and the REE pattern of allanite may change during crystallisation (Romer and Xiao 2005). Therefore, most magmatic allanite samples show variation in measured $^{147}Sm/^{144}Nd$ and $^{143}Nd/^{144}Nd$ (Table 7), but have consistent calculated initial $^{143}Nd/^{144}Nd$ values. Samples with a homogeneous initial $^{143}Nd/^{144}Nd$ can be used as a secondary reference material.

Allanite grains with low Sm/Nd ratios are ideal for *in situ* Sm-Nd isotope analysis. As summarised in Tables 7 and 8, the results obtained by LA-MC-ICP-MS (e.g., LE40010, LE2808, A007 and A011) are identical with the solution data. This demonstrates the feasibility of our *in situ* Sm-Nd analytical method. Combining their age, we can obtain the corresponding $\epsilon_{Nd}(t)$ values (Table 7 and 8). In brief, the data presented in this study indicate that reliable Sm-Nd isotopic composition can be obtained by LA-MC-ICP-MS.

Potential allanite reference materials for *in situ* Sm-Nd isotope measurement

Reference materials are crucial for *in situ* measurements in order to obtain accurate data. Ideal reference materials for *in situ* allanite Sm-Nd isotope analysis by LA-MC-ICP-MS should meet the following requirements: (a) have homogeneous $^{147}Sm/^{144}Nd$ and $^{143}Nd/^{144}Nd$ isotope ratios; (b) have a uniform distribution in Sm and Nd both within and between individual grains; (c) be free of inclusions and internal structures (e.g., cracks); (d) have a known crystallisation age; and (e) be available to the scientific community (Ma *et al.* 2019, Yang *et al.* 2019).

In this study, the long-term *in situ* $^{147}Sm/^{144}Nd$ and $^{143}Nd/^{144}Nd$ values of Daibosatsu allanite show very homogeneous composition. The mean $^{147}Sm/^{144}Nd$ ratio RSD is less than 2%. Therefore, Daibosatsu allanite is suitable as a reference material for *in situ* Sm-Nd measurement. The *in situ* Sm-Nd composition of LE40010 allanite shows limited variation in $^{147}Sm/^{144}Nd$ ratios with a mean RSD

Table 8.

Samarium and Nd mass fractions and $^{147}\text{Sm}/^{144}\text{Nd}$ and $^{143}\text{Nd}/^{144}\text{Nd}$ isotope ratios of allanite samples and previously characterised reference materials measured by ID-MC-ICP-MS in this study

Allanite	Sm ($\mu\text{g g}^{-1}$)	Nd ($\mu\text{g g}^{-1}$)	$^{147}\text{Sm}/^{144}\text{Nd}$	$^{143}\text{Nd}/^{144}\text{Nd}$	2SE	$^{143}\text{Nd}/^{144}\text{Nd}(t)$	$\epsilon_{\text{Nd}}(t)$		
LE2808 (~ 1100 Ma)									
1	9254	47122	0.1187	0.512225	0.000010	0.511368	2.94		
2	9138	46457	0.1189	0.512234	0.000010	0.511375	3.04		
Mean	9196	46789	0.1188	0.512230		0.511372	3.01		
2s	165	941	0.0003	0.000012		0.000010	0.20		
LE40010 (~ 2800 Ma)									
1	2339	24868	0.0568	0.510102	0.000009	0.509051	0.95		
2	2224	23567	0.0570	0.510113	0.000009	0.509059	1.11		
Mean	2281	24217	0.0569	0.510107		0.509055	1.03		
2s	163	1840	0.0002	0.000016		0.000011	0.22		
A007 (~ 1870 Ma)									
1	7554	41492	0.1100	0.511632	0.000009	0.510285	1.19		
2	7696	42488	0.1095	0.511635	0.000009	0.510295	1.38		
3	7772	41956	0.1120	0.511632	0.000009	0.510262	0.72		
4	7752	42307	0.1107	0.511627	0.000009	0.510272	0.92		
Mean	7693	42061	0.1106	0.511632		0.510279	1.05		
2s	197	878	0.0021	0.000007		0.000030	0.58		
A011 (~ 1160 Ma)									
1	2122	23764	0.0540	0.511710	0.000010	0.511299	3.10		
2	2264	25094	0.0545	0.511719	0.000008	0.511304	3.20		
3	2299	25450	0.0546	0.511725	0.000011	0.511309	3.31		
4	2268	25158	0.0545	0.511719	0.000009	0.511304	3.20		
Mean	2238	24866	0.0544	0.511718		0.511304	3.20		
2s	158	1502	0.0006	0.000013		0.000009	0.17		
CRM	Sm ($\mu\text{g g}^{-1}$) This study	Ref.	Nd ($\mu\text{g g}^{-1}$) This study	Ref.	$^{147}\text{Sm}/^{144}\text{Nd}$ This study	Ref.	$^{143}\text{Nd}/^{144}\text{Nd}$ This study	2SE	Ref.
BCR-2									
1	6.47	6.54 ^b 6.51 ^c	28.30	28.60 ^b 28.43 ^c	0.1382	0.1383 ^b 0.1385 ^c	0.512638	0.000007	0.512641 ^b 0.512637 ^c 0.512637 ^a
GSR-2									
1	3.20		17.60		0.1099		0.512395	0.000008	0.512382 ^d
GSR-3									
1	10.26		49.73		0.1248		0.512913	0.000009	0.512901 ^e
2	9.89		49.80		0.1200		0.512906	0.000008	0.512899 ^f
Mean	10.08		49.77		0.1224		0.512909		
2s	0.54		0.09		0.0067		0.000010		

$\epsilon_{\text{Nd}}(t)$ was calculated as an initial value with the age obtained by U-Pb dating of allanite in this study.

^a Weis *et al.* (2006), ^b Chu *et al.* (2009), ^c Yang *et al.* (2011), ^d Yang *et al.* (2020), ^e Fourny *et al.* (2016), ^f Bao *et al.* (2018).

of 0.71%. The *in situ* result of LE40010 agrees well with the solution-based data. Thus, the robustness of *in situ* results in combination with the coincidence of the *in situ* and solution-based results indicates that the Sm-Nd isotopic composition of LE40010 is reproducible and accurate. The Daibosatsu and LE40010 allanites can serve as excellent "external" reference materials for *in situ* Sm-Nd isotope measurements. Several of the studied allanites cannot be used as primary reference materials, but show very consistent and homogeneous initial $^{143}\text{Nd}/^{144}\text{Nd}$ isotope ratios, including CAP^b,

Tara, LE2808, A007, A011 and A012, which have the potential to serve as secondary reference materials. Sample SQ-51 shows a relatively large variation in initial $^{143}\text{Nd}/^{144}\text{Nd}$ values; therefore, it is not a good reference material candidate for LA-MC-ICP-MS analysis.

Conclusions

The obtained *in situ* allanite U-Th-Pb ages are consistent within uncertainty with literature values and our ID-TIMS

results. We recommend that LE40010 allanite has potential to serve as a primary reference material for *in situ* U-Pb dating, large dispersion on Th-Pb results still can make it a secondary reference material or *in situ* Th-Pb dating. CAP^b allanite could serve as primary reference material for *in situ* Th-Pb dating, but ideally, requires modern ID-TIMS characterisation. Furthermore, CAP^b, LE2808, A007, A011 and A012 can serve as secondary reference materials for *in situ* U-Pb dating. Daibosatsu allanite can be used as secondary reference material for Cenozoic Th-Pb dating to monitor data reproducibility, but its young age means it is not ideal to serve as primary reference material for U-Pb dating, due to the excess of ²⁰⁶Pb and a considerable amount of common Pb.

The ¹⁴⁷Sm/¹⁴⁴Nd and ¹⁴³Nd/¹⁴⁴Nd isotope ratios of natural allanite samples determined by *in situ* LA-MC-ICP-MS are consistent with the values determined by solution methods, demonstrating the reliability and robustness of the *in situ* Sm-Nd measurement protocol described herein. The Daibosatsu and LE40010 allanites show very homogeneous Sm-Nd isotopic compositions and are therefore, ideal primary reference materials for calibration of *in situ* Sm-Nd isotope measurements. CAP^b, Tara, LE2808, A007, A011 and A012 show homogeneous initial Nd isotopic compositions, which implies that they are suitable to serve as secondary reference materials for *in situ* Sm-Nd isotope measurements. Sample SQ-51 is heterogeneous in U-Pb age and Sm-Nd isotopic composition; thus, it is not a suitable candidate as a reference material for LA-MC-ICP-MS analysis.

Acknowledgments

This work was financially supported by the National Natural Science Foundation of China (Grants 41525012, 42173034 and 41688103). We thank two anonymous reviewers and editor S. Gilbert for thoughtful suggestions. The work of Ming Yang at GFZ was supported by the China Scholarship Council (202004910582). We are grateful to Marco Bum and Daniela Rubatto for providing the CAP^b and Tara allanite reference materials respectively. We thank Li X.C. and Ling X.X. for providing the allanite samples (SQ-51, A007, A011 and A012). We are indebted to Zhao H., Mao Q. and Ma Q. for their assistance during analytical procedures. The authors declare no conflict of interest.

Data availability statement

The data that support the findings of this study are available in the online supporting information of this article.

References

Bao Z.A., Zong C.L., Fang L.R., Yuan H.L., Chen K.Y. and Dai M.N. (2018)

Determination of Hf–Sr–Nd isotopic ratios by MC-ICP-MS using rapid acid digestion after flux-free fusion in geological materials. *Acta Geochemica*, 37, 244–256.

Barth A.P., Wooden J.L., Tosca R.M., Morrison J., Dawson D.L. and Hemly B.M. (1995)

Origin of gneisses in the aureole of the San Gabriel anorthosite complex and implications for the Proterozoic crustal evolution of southern California. *Tectonics*, 14, 736–752.

Barth S., Oberli F. and Meier M. (1989)

U-Th-Pb systematics of morphologically characterised zircon and allanite: A high-resolution isotopic study of the Alpine Rensen pluton (northern Italy). *Earth and Planetary Science Letters*, 95, 235–254.

Barth S., Oberli F. and Meier M. (1994)

Th-Pb versus U-Pb isotope systematics in allanite from co-genetic rhyolite and granodiorite: Implications for geochronology. *Earth and Planetary Science Letters*, 124, 149–159.

Bea F. (1996)

Residence of REE, Y, Th and U in granites and crustal protoliths: Implications for the chemistry of crustal melts. *Journal of Petrology*, 37, 521–552.

Beard J.S., Sorensen S.S. and Gieré R. (2006)

REE zoning in allanite related to changing partition coefficients during crystallization: Implications for REE behaviour in an epidote-bearing tonalite. *Mineralogical Magazine*, 70, 419–436.

Boston K.R., Rubatto D., Hermann J., Engi M. and Amelin Y. (2017)

Geochronology of accessory allanite and monazite in the Barrovian metamorphic sequence of the Central Alps, Switzerland. *Lithos*, 286, 502–518.

Boynnton W.V. (1984)

Geochemistry of the rare earth elements: Meteorite studies. In: Henderson P. (ed.), *Rare earth element geochemistry*. Elsevier (Amsterdam), 63–114.

Bum M., Lanari P., Pettke T. and Engi M. (2017)

Non-matrix-matched standardisation in LA-ICP-MS analysis: General approach, and application to allanite Th–U–Pb dating. *Journal of Analytical Atomic Spectrometry*, 32, 1359–1377.

Catlos E.J., Sorensen S.S. and Harrison T.M. (2000)

Th-Pb ion-microprobe dating of allanite. *American Mineralogist*, 85, 633–648.



references

- Chen W.T. and Zhou M.F. (2014)**
Ages and compositions of primary and secondary allanite from the Lala Fe–Cu deposit, SW China: Implications for multiple episodes of hydrothermal events. *Contributions to Mineralogy and Petrology*, 168, 1–20.
- Chu Z.Y., Chen F.K., Yang Y.H. and Guo J.H. (2009)**
Precise determination of Sm, Nd concentrations and Nd isotopic compositions at the nanogram level in geological samples by thermal ionization mass spectrometry. *Journal of Analytical Atomic Spectrometry*, 24, 1534–1544.
- Chu Z.Y., Wang M.J., Li C.F., Yang Y.H., Xu J.J., Wang W. and Guo J.H. (2019)**
Separation of Nd from geological samples by a single TODGA resin column for high precision Nd isotope analysis as NdO⁺ by TIMS. *Journal of Analytical Atomic Spectrometry*, 34, 2053–2060.
- Cox R.D., Wilton D.H.C. and Košler J. (2003)**
Laser-ablation U–Th–Pb *in situ* dating of zircon and allanite: an example from the October Harbour granite, central coastal Labrador, Canada. *The Canadian Mineralogist*, 44, 273–291.
- Cox S.E., Farley K.A. and Hemming S.R. (2012)**
Insights into the age of the Mono Lake Excursion and magmatic crystal residence time from (U–Th)/He and ²³⁰Th dating of volcanic allanite. *Earth and Planetary Science Letters*, 319–320, 178–184.
- Darling J.R., Storey C.D. and Engi M. (2012)**
Allanite U–Th–Pb geochronology by laser ablation ICP–MS. *Chemical Geology*, 292, 103–115.
- Deng X.D., Li J.W. and Wen G. (2014)**
Dating iron skarn mineralization using hydrothermal allanite-(La) U–Th–Pb isotopes by laser ablation ICP–MS. *Chemical Geology*, 382, 95–110.
- Dollase W.A. (1971)**
Refinement of the crystal structures of epidote, allanite and hancockite. *American Mineralogist*, 56, 447–464.
- Dubois J.C., Retali G. and Cesario J. (1992)**
Isotopic analysis of rare earth elements by total vaporization of samples in thermal ionization mass spectrometry. *International Journal of Mass Spectrometry and Ion Processes*, 120, 163–177.
- Engi M. (2017)**
Petrochronology based on REE-minerals monazite, allanite, xenotime, apatite: Methods and applications. *Reviews in Mineralogy and Geochemistry*, 86, 365–418.
- Fisher C.M., McFarlane C.R.M., Hanchar J.M., Schmitz M.D., Sylvester P.J., Lam R. and Longerich H.P. (2011)**
Sm–Nd isotope systematics by laser ablation-multicollector-inductively coupled plasma-mass spectrometry: Methods and potential natural and synthetic reference materials. *Chemical Geology*, 284, 1–20.
- Förster H.-J. and Romer R.L. (2010)**
Carboniferous magmatism. In: Linnemann U. and Romer R.L. (eds), *Pre-Mesozoic geology of Saxo-Thuringia – From the Cadomian active margin to the Variscan orogen*. Schweizerbart (Stuttgart), 287–308.
- Foster G.L. and Vance D. (2006)**
In situ Nd isotopic analysis of geological materials by laser ablation MC–ICP–MS. *Journal of Analytical Atomic Spectrometry*, 21, 288–296.
- Foumy A., Weis D. and Scoates J.S. (2016)**
Comprehensive Pb–Sr–Nd–Hf isotopic, trace element, and mineralogical characterisation of mafic to ultramafic rock reference materials. *Geochemistry Geophysics Geosystems*, 17, 739–773.
- Fu Y., Sun X.M., Li D.F., Lin H. and Lai C. (2017)**
LA–ICP–MS U–Th–Pb dating and trace element geochemistry of allanite: Implications on the different skarn metallogenesis between the Giant Beiya Au and Machangqing Cu–Mo–(Au) deposits in Yunnan, SW China. *Minerals*, 7, 251.
- Gas'kov I.V., Anh T.T., Hoa T.T., Dung P.T., Nevol'ko P.A. and Can P.N. (2012)**
The Sin Quyen Cu–Fe–Au–REE deposit (northern Vietnam): Composition and formation conditions. *Russian Geology Geophysics*, 53, 442–456.
- Gerstenberger H. and Haase G. (1997)**
A highly effective emitter substance for mass spectrometric Pb isotope ratio determinations. *Chemical Geology*, 136, 309–312.
- Gieré R. (1986)**
Zirconolite, allanite and hoegbomite in a marble skarn from the Bergell contact aureole: Implications for mobility of Ti, Zr and REE. *Contributions to Mineralogy and Petrology*, 93, 459–470.
- Gieré R. and Sorensen S.S. (2004)**
Allanite and other REE-rich epidote-group minerals. *Reviews in Mineralogy and Geochemistry*, 56, 431–493.
- Gonçalves G.O., Lana C., Scholz R., Buick I.S., Gerdes A., Kamo S.L., Corfu F., Rubatto D., Wiedenbeck M., Nalini H.A. Jr. and Oliveira L.C.A. (2018)**
The diamantina monazite: A new low-Th reference material for microanalysis. *Geostandards and Geoanalytical Research*, 42, 25–47.
- Gregory C.J., McFarlane C.R.M., Hermann J. and Rubatto D. (2009)**
Tracing the evolution of calc-alkaline magmas: *In-situ* Sm–Nd isotope studies of accessory minerals in the Bergell Igneous Complex, Italy. *Chemical Geology*, 260, 73–86.
- Gregory C.J., Rubatto D., Allen C.M., Williams I.S., Hermann J. and Ireland T. (2007)**
Allanite micro-geochronology: A LA–ICP–MS and SHRIMP U–Th–Pb study. *Chemical Geology*, 245, 162–182.
- Gregory C.J., Rubatto D., Hermann J., Berger A. and Engi M. (2012)**
Allanite behaviour during incipient melting in the southern Central Alps. *Geochimica et Cosmochimica Acta*, 84, 433–458.

references

Griffin W.L., Powell W.J., Pearson N.J. and O'Reilly S.Y. (2008)

GLITTER: Data reduction software for laser ablation ICP-MS. In: Sylvester P. (ed.), *Laser Ablation-ICP-MS in the Earth sciences: Current practices and outstanding issues*. Mineralogical Association of Canada, Short Course, 40, 308–311.

Gromet L.P. and Silver L.T. (1983)

Rare earth element distributions among minerals in a granodiorite and their petrogenetic implications. *Geochimica et Cosmochimica Acta*, 47, 925–939.

Gu X.P. (1989)

Allanite as the indicator of the oxygen fugacity of granite magmas. *Minerals and Rocks*, 9, 26–32. (in Chinese with English abstract)

Guo H.H., Xiao Y.L., Gu X.P., Huang J., Hou Z.H. and Liu H.Y. (2014)

LA-ICP-MS allanite U-Th-Pb geochronology study on Guangdong Xinfeng REE-rich granite. *Acta Geologica Sinica*, 88, 1025–1037. (in Chinese with English abstract)

Guo H.H., Xiao Y.L., Xu L.J., Sun H., Huang J. and Hou Z.H. (2017)

Origin of allanite in gneiss and granite in the Dabie orogenic belt, Central East China. *Journal of Asian Earth Sciences*, 135, 243–256.

Hammerli J., Kemp A.I.S. and Spandler C. (2014)

Neodymium isotope equilibration during crustal metamorphism revealed by *in situ* microanalysis of REE-rich accessory minerals. *Earth and Planetary Science Letters*, 392, 133–142.

Hammerli J., Kemp A.I.S. and Whitehouse M.J. (2019)

In situ trace element and Sm-Nd isotope analysis of accessory minerals in an Eoarchean tonalitic gneiss from Greenland: Implications for Hf and Nd isotope decoupling in Earth's ancient rocks. *Chemical Geology*, 524, 394–405.

Hemann J. (2002)

Allanite: Thorium and light rare earth element carrier in subducted crust. *Chemical Geology*, 192, 289–306.

Hiess J., Condon D.J., Mclean N. and Noble S.R. (2012)

$^{238}\text{U}/^{235}\text{U}$ systematics in terrestrial uranium-bearing minerals. *Science*, 335, 1610–1614.

Holstam D., Andersson U.B., Broman C. and Mansfeld J. (2014)

Origin of REE mineralization in the Bastnäs-type Fe-REE-(Cu-Mo-Bi-Au) deposits, Bergslagen, Sweden. *Mineralium Deposita*, 49, 933–966.

Horstwood M.S.A., Košler J., Gehrels G., Jackson S.E., McLean N.M., Paton C., Pearson N., Sircombe K., Sylvester P., Vermeesch P., Bowring J.F., Condon D.J. and Schoene B. (2016)

Community-derived standards for LA-ICP-MS U-(Th)-Pb geochronology – Uncertainty propagation, age interpretation and data reporting. *Geostandards and Geoanalytical Research*, 40, 311–332.

Hoshino M., Kinata M., Nishida N., Kyono A., Shimizu M. and Takizawa S. (2005)

The chemistry of allanite from the Daibosatsu Pass, Yamanashi, Japan. *Mineralogical Magazine*, 69, 403–424.

Ickert R.B. and Williams I.S. (2011)

U-Pb zircon geochronology of Silurian-Devonian granites in southeastern Australia: Implications for the timing of the Benambran Orogeny and the I-S dichotomy. *Australian Journal of Earth Sciences*, 58, 501–516.

Iizuka T., Eggins S.M., McCulloch M.T., Kinsley L.P.J. and Mortimer G.E. (2011)

Precise and accurate determination of $^{147}\text{Sm}/^{144}\text{Nd}$ and $^{143}\text{Nd}/^{144}\text{Nd}$ in monazite using laser ablation-MC-ICP-MS. *Chemical Geology*, 282, 45–57.

Isnard H., Brennetot R., Caussignac C., Caussignac N. and Chartier F. (2005)

Investigations for determination of Gd and Sm isotopic compositions in spent nuclear fuels samples by MC ICP-MS. *International Journal of Mass Spectrometry*, 246, 66–73.

Jacobsen S.B. and Wasserburg G.J. (1980)

Sm-Nd isotopic evolution of chondrites. *Earth and Planetary Science Letters*, 50, 139–155.

Jaffey A.H., Flynn K.F., Glendenin L.E., Bentley W.C. and Essling A.M. (1971)

Precision measurement of half-lives and specific activities of ^{235}U and ^{238}U . *Physical Review C*, 4, 1889–1906.

Janots E., Engi M., Berger A., Allaz J., Schwarz J.O. and Spandler C. (2012)

Prograde metamorphic sequence of REE minerals in pelitic rocks of the Central Alps: Implications for allanite–monazite–xenotime phase relations from 250 to 610 °C. *Journal of Metamorphic Geology*, 26, 509–526.

Janots E., Engi M., Rubatto D., Berger A., Gregory C. and Rahn M. (2009)

Metamorphic rates in collisional orogeny from *in situ* allanite and monazite dating. *Geology*, 37, 11–14.

Jochum K.P., Weis U., Stoll B., Kuzmin D., Yang Q.C., Raczek I., Jacob D.E., Stracke A., Birbaum K., Frick D.A., Günther D. and Enzweiler J. (2011)

Determination of reference values for NIST SRM 610–617 glasses following ISO guidelines. *Geostandards and Geoanalytical Research*, 35, 397–429.

Klimm K., Blundy J.D. and Green T.H. (2008)

Trace element partitioning and accessory phase saturation during H₂O-saturated melting of basalt with implications for subduction zone chemical fluxes. *Journal of Petrology*, 49, 523–553.



references

Korh A.E. (2014)

Ablation behaviour of allanites during U-Th-Pb dating using a quadrupole ICP-MS coupled to a 193 nm excimer laser. *Chemical Geology*, 371, 46–59.

Krogh T.E. (1973)

A low-contamination method for hydrothermal decomposition of zircon and extraction of U and Pb for isotopic age determinations. *Geochimica et Cosmochimica Acta*, 37, 485–494.

Kroner U. and Romer R.L. (2013)

Two plates – Many subduction zones: The Variscan orogeny reconsidered. *Gondwana Research*, 24, 298–329.

Lee D.E. and Bastron H. (1967)

Fractionation of rare-earth elements in allanite and monazite as related to geology of the Mt. Wheeler mine area, Nevada. *Geochimica et Cosmochimica Acta*, 31, 339–356.

Li J.W., Deng X.D., Zhou M.F., Liu Y.S., Zhao X.F. and Guo J.L. (2010)

Laser ablation ICP-MS titanite U-Th-Pb dating of hydrothermal ore deposits: A case study of the Tonglushan Cu-Fe-Au skarn deposit, SE Hubei Province, China. *Chemical Geology*, 270, 56–67.

Li X.C., Zhao X.F., Zhou M.F., Chen W.T. and Cho Z.Y. (2015)

Fluid inclusion and isotopic constraints on the origin of the Paleoproterozoic Yinachang Fe-Cu-(REE) deposit, Southwest China. *Economic Geology*, 110, 1339–1369.

Li X.C., Zhou M.F., Chen W.T., Zhao X.F. and Tran M.D. (2018)

Uranium-lead dating of hydrothermal zircon and monazite from the Sin Quyen Fe-Cu-REE-Au-(U) deposit, northwestern Vietnam. *Mineralium Deposita*, 53, 399–416.

Liao X., Li Q.L., Whitehouse M.J., Yang Y.H. and Liu Y. (2020)

Allanite U-Th-Pb geochronology by ion microprobe. *Journal of Analytical Atomic Spectrometry*, 35, 489–497.

Lin J., Liu Y.S., Yang Y.H. and Hu Z.C. (2016)

Calibration and correction of LA-ICP-MS and LA-MC-ICP-MS analyses for element contents and isotopic ratios. *Solid Earth Sciences*, 1, 5–27.

Linders W. (2016)

U-Pb geochronology and geochemistry of host rocks to the Bastnäs-type REE mineralization in the Riddarhyttan area, west central Bergslagen, Sweden. *Dissertations in Geology at Lund University*, 8–21.

Liu Z.C., Wu F.Y., Yang Y.H., Yang J.H. and Wilde S.A. (2012)

Neodymium isotopic compositions of the standard monazites used in U-Th-Pb geochronology. *Chemical Geology*, 334, 221–239.

Ludwig K.R. (2003)

ISOPLOT 3.0 – A geochronological toolkit for Microsoft

Excel. Berkeley Geochronology Center Special Publication, No. 4, (Berkeley, USA), 70pp.

Lugmair G.W. and Marti K. (1978)

Lunar initial $^{143}\text{Nd}/^{144}\text{Nd}$: Differential evolution of the lunar crust and mantle. *Earth and Planetary Science Letters*, 39, 349–357.

Ma Q., Evans N.J., Ling X.X., Yang J.H., Wu F.Y., Zhao Z.D. and Yang Y.H. (2019)

Natural titanite reference materials for *in situ* U-Pb and Sm-Nd isotopic measurements by LA-(MC)-ICP-MS. *Geostandards and Geoanalytical Research*, 43, 355–384.

Mattinson J.M. (1987)

U-Pb ages of zircons: A basic examination of error propagation. *Chemical Geology*, 66, 151–162.

McFarlane C.R.M. (2016)

Allanite U-Pb geochronology by 193 nm LA ICP-MS using NIST610 glass for external calibration. *Chemical Geology*, 438, 91–102.

McFarlane C.R.M. and McCulloch M.T. (2007)

Coupling of *in-situ* Sm-Nd systematics and U-Pb dating of monazite and allanite with applications to crustal evolution studies. *Chemical Geology*, 245, 45–60.

McFarlane C.R.M. and McCulloch M.T. (2008)

Sm-Nd and Sr isotope systematics in LREE-rich accessory minerals using LA-MC-ICP-MS. *Mineralogical Association of Canada*, 40, 117–133.

Montel J.M. (1993)

A model for monazite/melt equilibrium and application to the generation of granitic magmas. *Chemical Geology*, 110, 127–146.

O’Nions R.K., Hamilton P.J. and Evensen N.M. (1977)

Variations in $^{143}\text{Nd}/^{144}\text{Nd}$ and $^{87}\text{Sr}/^{86}\text{Sr}$ ratios in oceanic basalts. *Earth and Planetary Science Letters*, 34, 13–22.

Oberli F., Meier M., Berger A., Rosenberg C.L. and Gieré R. (2004)

U-Th-Pb and $^{230}\text{Th}/^{238}\text{U}$ disequilibrium isotope systematics: Precise accessory mineral chronology and melt evolution tracing in the Alpine Bergell intrusion. *Geochimica et Cosmochimica Acta*, 68, 2543–2560.

Oliver N.H.S., Pearson P.J., Holcombe R.J. and Ord A. (1999)

Mary Kathleen metamorphic-hydrothermal uranium-rare-earth element deposit: Ore genesis and numerical model of coupled deformation and fluid flow. *Journal of the Geological Society of Australia*, 46, 467–484.

Parrish R.R., Gough S.J., Searle M.P. and Waters D.J. (2006)

Plate velocity exhumation of ultrahigh-pressure eclogites in the Pakistan Himalaya. *Geology*, 34, 989–992.

Petrík I., Broska I., Lipka J. and Šiman P. (1995)

Granitoid allanite-(Ce): Substitution relations, redox conditions and REE distributions (on an example of I-type granitoids, western Carpathians, Slovakia). *Geologica Carpathica*, 46, 79–94.

references

- Robinson D.M. and Miller C.F. (1999)**
Record of magma chamber processes preserved in accessory mineral assemblages, Aztec Wash Pluton, Nevada. *American Mineralogist*, **84**, 1346–1353.
- Romer R.L. and Lüders V. (2006)**
Direct dating of hydrothermal W mineralization: U-Pb age for hübnerite (MnWO₄), Sweet Home Mine, Colorado. *Geochimica et Cosmochimica Acta*, **70**, 4725–4733.
- Romer R.L. and Wright J.E. (1993)**
Lead mobilization during tectonic reactivation of the western Baltic Shield. *Geochimica et Cosmochimica Acta*, **57**, 2555–2570.
- Romer R.L. and Xiao Y. (2005)**
Initial Pb-Sr(Nd) isotopic heterogeneity in a single allanite-epidote crystal: Implications of reaction history for the dating of minerals with low parent-to-daughter ratios. *Contributions to Mineralogy and Petrology*, **148**, 662–674.
- Rötzler K. and Plessen B. (2010)**
The Erzgebirge: A pile of ultrahigh- to low-pressure nappes of Early Palaeozoic rocks and their Cadomian basement. In: Linnemann U. and Romer R.L. (eds), *Pre-mesozoic geology of Saxo-Thuringia – From the Cadomian active margin to the Variscan orogen*. Schweizerbart (Stuttgart), 253–270.
- Rubatto D., Regis D., Hermann J., Boston K., Engi M., Beltrando M. and McAlpine S.R.B. (2011)**
Yo-yo subduction recorded by accessory minerals in the Italian western Alps. *Nature Geoscience*, **4**, 338–342.
- Schaltegger U. and Davies J. (2017)**
Petrochronology of zircon and baddeleyite in igneous rocks: Reconstructing magmatic processes at high temporal resolution. *Reviews in Mineralogy and Geochemistry*, **83**, 297–328.
- Schmid R., Romer R.L., Franz L., Oberhänsli R. and Martinotti G. (2003)**
Basement-cover sequences within the UHP unit of the Dabie Shan. *Journal of Metamorphic Geology*, **21**, 531–538.
- Searle M.P., Roberts N.M.W., Chung S.-L., Lee Y.-H., Cook K.L., Elliott J.R., Weller O.M., St-Onge M.R., Xu X.-W., Tan X.-B. and Li K. (2016)**
Age and anatomy of the Gongga Shan batholith, eastern Tibetan Plateau, and its relationship to the active Xianshuihe fault. *Geosphere*, **12**, 948–970.
- Silver L.T., McKinney C.R., Deutsch S. and Bolinger J. (1963)**
Precambrian age determinations in the western San Gabriel Mountains, California. *Journal of Geology*, **71**, 196–214.
- Sláma J., Košler J., Condon D.J., Crowley J.L., Gerdes A., Hanchar J.M., Horstwood M.S.A., Morris G.A., Nasdala L., Norberg N., Schaltegger U., Schoene B., Tubrett M.N. and Whitehouse M.J. (2008)**
Plešovice zircon – A new natural reference material for U-Pb and Hf isotopic microanalysis. *Chemical Geology*, **249**, 1–35.
- Smith M.P., Storey C.D., Jeffries T.E. and Ryan C. (2009)**
In situ U-Pb and trace element analysis of accessory minerals in the Kiruna District, Norrbotten, Sweden: New constraints on the timing and origin of mineralization. *Journal of Petrology*, **50**, 2063–2094.
- Smye A.J., Bickle M.J., Holland T.J.B., Parrish R.R. and Condon D.J. (2011)**
Rapid formation and exhumation of the youngest Alpine eclogites: A thermal conundrum to Barrovian metamorphism. *Earth and Planetary Science Letters*, **306**, 193–204.
- Smye A.J., Roberts N.M.W., Condon D.J., Horstwood M.S.A. and Parrish R.R. (2014)**
Characterising the U-Th-Pb systematics of allanite by ID and LA-ICP-MS: Implications for geochronology. *Geochimica et Cosmochimica Acta*, **135**, 1–28.
- Soder C. and Romer R.L. (2018)**
Post-collisional potassic-ultrapotassic magmatism of the Variscan Orogen: Implications for mantle metasomatism during continental subduction. *Journal of Petrology*, **59**, 1007–1034.
- Spandler C., Hammerli J. and Pirard C. (2018)**
Neodymium isotope disequilibria in subducted sediments, and potential consequences for subduction-zone recycling. *Geology*, **46**, 815–818.
- Spandler C., Hammerli J., Sha P., Hilbert-Wolf H., Hu Y., Roberts E. and Schmitz M. (2016)**
MKED1: A new titanite standard for *in situ* analysis of Sm-Nd isotopes and U-Pb geochronology. *Chemical Geology*, **425**, 110–126.
- Spandler C., Hermann J., Arculus R. and Mavrogenes J. (2003)**
Redistribution of trace elements during prograde metamorphism from lawsonite blueschist to eclogite facies; implications for deep subduction-zone processes. *Contributions to Mineralogy and Petrology*, **146**, 205–222.
- Spürgin S., Selbekk R. S., and Lundmark A. M. (2009)**
Mineralogy and geological setting of allanite-(Ce)-pegmatites in western Hurrungane, Jotun Nappe Complex, Norway: An EMP and ID-TIMS study. *Norsk Geologisk Tidsskrift*, **89**, 341–356.
- Stacey J.S. and Kramers J.D. (1975)**
Approximation of terrestrial lead isotope evolution by a two-stage model. *Earth and Planetary Science Letters*, **26**, 207–221.
- Stephens M.B. and Jansson N.F. (2020)**
Chapter 6 Paleoproterozoic (1.9–1.8 Ga) syn-orogenic magmatism, sedimentation and mineralization in the Bergslagen lithotectonic unit, Svecokarelian orogen. *Geological Society of London Memoir*, **50**, 155–206.



references

- Su Z.K., Zhao X.F., Li X.C., Zhou M.F., Kennedy A.L., Zi J.W., Spandler C. and Yang Y.H. (2021) Unraveling mineralization and multistage hydrothermal overprinting histories by integrated *in situ* U-Pb and Sm-Nd isotopes in a Paleoproterozoic breccia-hosted iron oxide copper-gold deposit, SW China. *Economic Geology*, 116, 1687–1710.
- Thakur S.S., Madhavan K., Patel S.C., Rao D.R., Sinha A.K., Pandey S. and Nandini P. (2018) Yttrium-zoning in garnet and stability of allanite in metapelites from the Main Central Thrust Zone and adjacent higher Himalayan Crystallines along the Alaknanda Valley, NW Himalaya. *Lithos*, 320–321, 1–19.
- von Blanckenburg F. (1992) Combined high-precision chronometry and geochemical tracing using accessory minerals: Applied to the Central-Alpine Bergell intrusion (central Europe). *Chemical Geology*, 100, 19–40.
- Vonlanthen P., Fitz Gerald J.D., Rubatto D. and Hemann J. (2012) Recrystallization rims in zircon (Valle d'Arbedo, Switzerland): An integrated cathodoluminescence, LA-ICP-MS, SHRIMP, and TEM study. *American Mineralogist*, 97, 369–377.
- Walters A.S., Goodenough K.M., Hughes H.S.R., Roberts N.M.W., Gunn A.G., Rushton J. and Lacinska A. (2013) Enrichment of rare earth elements during magmatic and post-magmatic processes: A case study from the Loch Loyal Syenite Complex, northern Scotland. *Contributions to Mineralogy and Petrology*, 166, 1177–1202.
- Wasserburg G.J., Jacobsen S.B., DePaolo D.J., McCulloch M.T. and Wen T. (1981) Precise determination of Sm/Nd ratios, Sm and Nd isotopic abundances in standard solutions. *Geochimica et Cosmochimica Acta*, 45, 2311–2323.
- Weis D., Kieffer B., Maerschalk C., Barling J., de Jong J., Williams G.A., Hanano D., Pretorius W., Mattioli N., Scoates J.S., Goolaerts A., Friedman R.M. and Mahoney J.B. (2006) High-precision isotopic characterisation of USGS reference materials by TIMS and MC-ICP-MS. *Geochemistry, Geophysics, Geosystems*, 7, Q08006.
- Wiedenbeck M., Hanchar J.M., Peck W.H., Sylvester P., Valley J., Whitehouse M., Kronz A., Morishita Y., Nasdala L., Fiebig J., Franchi I., Girard J.P., Greenwood R.C., Hinton R., Kita N., Mason P.R.D., Norman M., Ogasawara M., Piccoli P.M., Rhede D., Satoh H., Schulz-Dobrick B., Skår Ø., Spicuzza M.J., Terada K., Tindle A., Togashi S., Vennemann T., Xie Q. and Zheng Y.F. (2004) Further characterisation of the 91500 zircon crystal. *Geostandards and Geoanalytical Research*, 28, 9–39.
- Wing B.A., Ferry J.M. and Harrison T.M. (2003) Prograde destruction and formation of monazite and allanite during contact and regional metamorphism of pelites: Petrology and geochronology. *Contributions to Mineralogy and Petrology*, 145, 228–250.
- Wones D.R. (1989) Significance of the assemblage titanite + magnetite + quartz in granitic rocks. *American Mineralogist*, 74, 744–749.
- Wu F.Y., Yang Y.H., Xie L.W., Yang J.H. and Xu P. (2006) Hf isotopic compositions of the standard zircons and baddeleyites used in U-Pb geochronology. *Chemical Geology*, 234, 105–126.
- Wu S.T., Yang M., Yang Y.H., Xie L.W., Huang C., Wang H. and Yang J.H. (2020) Improved *in situ* zircon U-Pb dating at high spatial resolution (5–16 μm) by laser ablation-single collector-sector field-ICP-MS using jet sample and X skimmer cones. *International Journal of Mass Spectrometry*, 456, 116394.
- Yang Y.H., Chu Z.Y., Wu F.Y., Xie L.W. and Yang J.H. (2011) Precise and accurate determination of Sm, Nd concentrations and Nd isotopic compositions in geological samples by MC-ICP-MS. *Journal of Analytical Atomic Spectrometry*, 26, 1237–1244.
- Yang Y.H., Sun J.F., Xie L.W., Fan H.R. and Wu F.Y. (2008) *In situ* Nd isotopic measurement of natural geological materials by LA-MC-ICP-MS. *Chinese Science Bulletin*, 53, 1062–1070.
- Yang Y.H., Wu F.Y., Chu Z.Y., Xie L.W. and Yang J.H. (2013) High-precision simultaneous determination of $^{147}\text{Sm}/^{144}\text{Nd}$ and $^{143}\text{Nd}/^{144}\text{Nd}$ ratios in Sm-Nd mixtures using multicollector inductively coupled plasma-mass spectrometry and its comparison to isotope dilution analysis. *Spectrochimica Acta Part B*, 79–80, 82–87.
- Yang Y.H., Wu F.Y., Li Q.L., Rojas-Agramonte Y., Yang J.H., Li Y., Xie L.W., Huang C., Fan H.R., Zhao Z.F. and Xu C. (2019) *In situ* U-Th-Pb dating and Sr-Nd isotope analysis of bastnäsite by LA-(MC)-ICP-MS. *Geostandards and Geoanalytical Research*, 43, 543–565.
- Yang Y.H., Wu F.Y., Wilde S.A., Liu X.M., Zhang Y.B., Xie L.W. and Yang J.H. (2009) *In situ* perovskite Sr-Nd isotopic constraints on the petrogenesis of the Ordovician Mengyin kimberlites in the North China Craton. *Chemical Geology*, 264, 24–42.
- Yang Y.H., Wu F.Y., Xie L.W. and Zhang Y.B. (2010) High-precision measurements of the $^{143}\text{Nd}/^{144}\text{Nd}$ isotope ratio in certified reference materials without Nd and Sm separation by multiple collector inductively coupled plasma-mass spectrometry. *Analytical Letters*, 43, 142–150.
- Yang Y.H., Wu F.Y., Yang J.H., Chew D.M., Xie L.W., Chu Z.Y., Zhang Y.B. and Huang C. (2014) Sr and Nd isotopic compositions of apatite reference materials used in U-Th-Pb geochronology. *Chemical Geology*, 385, 35–55.
- Yang Y.H., Yang M., Jochum K.P., Wu S.T., Zhao H., Xie L.W., Huang C., Zhan X.C., Yang J.H. and Wu F.Y. (2020) High-precision Sr-Nd-Hf-Pb isotopic composition of Chinese geological standard glasses CGSG-1, CGSG-2, CGSG-4 and CGSG-5 reference materials by MC-ICP-MS and TIMS. *Geostandards and Geoanalytical Research*, 44, 567–579.

references

Zhu H.P., Nie F.J., Shi M.F., Nie F., Wang H. and Yang Y.F. (2015)

Gaint Sin Quyen Cu-Au-Fe-REE deposit, northwestern Vietnam. *Mineral Deposits*, 34, 632–636. (in Chinese)

Supporting information

The following supporting information may be found in the online version of this article:

Table S1. Individual EPMA data of allanite samples investigated in this study.

Table S2. Individual trace element data of allanite samples obtained by LA-ICP-MS investigated in this study.

Table S3. Individual age data of allanite samples obtained by LA-ICP-MS investigated in this study.

Table S4. Individual Sm-Nd data of allanite samples obtained by LA-MC-ICP-MS investigated in this study.

This material is available from: <http://onlinelibrary.wiley.com/doi/10.1111/ggr.12417/abstract> (This link will take you to the article abstract).